EVALUATION OF RELATIVE PERMEABILITY OF OIL- WATER SYSTEMS IN NATURAL FRACTURES

A Thesis

by

DERON RASHAD ARCENEAUX

Submitted to the Office of Graduate and Professional Studies of
Texas A&M University
in partial fulfillment of the requirements for the degree of

MASTER OF SCIENCE

Chair of Committee,	A. Daniel Hill
Co-Chair of Committee,	Ding Zhu
Committee Member,	Arthur Donovan
Head of Department,	Jeff Spath

August 2020

Major Subject: Petroleum Engineering

ABSTRACT

This thesis is aimed to develop an understanding of relative permeability in fractures of oil-water systems. Currently, two-phase flow behavior across unpropped and propped fractures is not well known. As a result, reservoir modeling using computational simulation for the area involving fractures typically utilizes straight-line relative permeability and zero capillary pressure in fractures. Nonetheless, several experiments have shown that both viscous and capillary dominated flows can be predicted in naturally fractured reservoirs where non-straight-line relative permeability must be used to model such reservoirs correctly.

The experimental analyses performed in this thesis were carried out using the outcrop core from the Eagle Ford shale formation. The outcrop Eagle Ford rock was cored into four 1.5" diameter by 6" cores and saw cut to generate a natural fracture on each core sample. The cores were then saturated in Eagle Ford formation oil at reservoir temperature for a minimum of 30 days before any experiments.

The steady-state method was applied to measure the oil-water relative permeability. Eagle Ford formation oil and reconstituted brine with and without surfactants were used as the test fluids. The measurements were recorded at effective fracture closure stress and reservoir temperature. Also, real-time measurements of density, pressure, and flow rate will be logged throughout the entire duration of each test. Fluid saturations within the fracture were calculated using the mass continuity equation. Results from the experiment were analyzed using Darcy's Law, and a visible relationship was found between saturation and relative permeability. The determined relative permeability curves closely follow the generalized Brooks-Corey

relationship for oil-water systems. In comparison, there was a significant difference between the oil-water only systems and the oil-water surfactant systems in the relative permeability curves.

Results from the experiments conducted indicate the potential for surfactant additives to significantly improve the relative permeability of oil by as much as 26%. Also, the results show the use of the straight-line relative permeability to predict oil recovery would result in a high percent error.

DEDICATION

"If my mind can conceive it, and my heart can believe it, then I can achieve it."

-Muhammad Ali

I dedicate my thesis work to my family and many friends. Special thanks to my parents Ronald and Desiree Arceneaux; none of this is possible without having you in my life. Thank you for all the support and sacrifices you have made in your life to ensure I would be successful. My sister Alyssa, thank you for always being supportive and continue to pursue your dreams; you will always have our full support with anything you do in life. I also dedicate this to my grandparents Irvin Arceneaux and Stella Nichols, for showing me how valuable getting an education is and the benefits of having one. To my many aunts, uncles, and cousins, thank you for guiding me throughout my life and academic career with your advice and support.

To my many friends, thank you for helping get through graduate school and making school enjoyable. Lastly, special thanks to my best friend, Brandi Houston, for being there for me throughout the entire master's program.

Thank you to all of you for standing by my side during the process of not only earning this master's degree but throughout my life.

ACKNOWLEDGEMENTS

I would like to thank my committee chair, Dr. Hill, and co-chair Dr. Zhu for being very patient with me, along with their guidance and support throughout this research. I am very appreciative of the opportunity they've given to be a part of their research group and learn from the most distinguished professors petroleum engineering has to offer. I'd also like to thank Dr. Donovan for serving as a member of my committee. I learned a lot from Dr. Donovan when I took his stratigraphy class, where I learned how to read well logs and interpret where different formations were located.

Thanks also go to my friends and colleagues for making my time at Texas A&M University a great experience. I would like to give special thanks to Dante Guerra for helping me throughout my research and being patient with me anytime I had questions. I would also like to thank other students in the research group that helped me be successful: Robert Shirley, Michael Luketich, Allyx Copeland, Julian Uribe, James Fernandez, Jimmy Xiao, and Tohoko Tajima.

Lastly, I'd like to thank the department faculty and staff, John Maldonado, Sr., and Don Conlee, for helping me assemble and provide maintenance on lab equipment throughout my research.

CONTRIBUTORS AND FUNDING SOURCES

This work was supervised by a thesis committee consisting of Professor A. Daniel Hill, primary advisor, and Professor Ding Zhu, co-advisor of the Harold Vance Department of Petroleum Engineering and Professor Arthur Donovan of the Department of Geology and Geophysics.

The data analyzed for Section 2.2.1 was provided by student Igor Ivanishin under the supervision of Dr. Nasr-El-Din of the Harold Vance Department of Petroleum Engineering. The data analyzed for Section 2.3.3 was provided by student Rakananda Saputra under the supervision of Dr. David Schechter of the Harold Vance Department of Petroleum Engineering.

All other work conducted for the thesis was completed by the student independently.

Graduate study was supported by a fellowship from Texas A&M University and a master's research fellowship from the National GEM Consortium.

This work was also made possible in part by Marathon Oil Corporation under TEES project number 28-408800-00001. Its contents are solely the responsibility of the authors and do not necessarily represent the official views of the Marathon Oil Corporation.

NOMENCLATURE

A	Fracture cross-sectional area, L^2, (cm^2)
a_f	Fracture aperture, L, (cm)
C_o	Corey exponent for oil
C_w	Corey exponent for water
D_h	Hydraulic diameter, (cm)
F_o	Oil fraction, (fraction)
F_w	Water fraction, (fraction)
k	Absolute permeability, L^2, (md)
k_{eo}	Effective permeability to oil, L^2 , (md)
k_{ew}	Effective permeability to water, L^2 , (md)
k_r	Relative permeability, (fraction)
k_{ro}	Relative permeability to oil, (fraction)
k_{rw}	Relative permeability to water, (fraction)
$k_{ro(S_{w\,min})}$	Relative permeability to oil at min. water saturation, (fraction)
$k_{rw(S_{or})}$	Relative permeability to water at residual oil saturation, (fraction)
L	Core length, L, (cm)
$\dot{m}_m$	Mass flow rate of mixture, Mt^{-1}, (g/min.)
θ	Contact Angle, (°)
P	Pressure, $ML^{-1}\,t^{-2}$, (psig)
ΔP_{ss}	Differential pressure at steady state, $ML^{-1}t^{-2}$, (psig)

P_c	Capillary Pressure, (mN/m/r)
$P_{confining}$	Confining pressure, $ML^{-1}\ t^{-2}$, (psig)
P_{wet}	Wetted perimeter in contact with fluid, (cm)
ρ_m	Fluid density of mixture, ML^{-3}, (g/cm^3)
ρ_o	Fluid density of oil, ML^{-3}, (g/cm^3)
ρ_w	Fluid density of water, ML^{-3}, (g/cm^3)
Q	Volumetric flow rate, L^3t^{-1}, (mL/min.)
σ	Oil-water interfacial tension, (mN/m)
R_e	Reynolds Number
S_o	Oil saturation, (fraction)
S_{or}	Residual oil saturation, (fraction)
S_w	Water saturation, (fraction)
S_{wi}	Initial water saturation, (fraction)
S_{wirr}	Irreducible water saturation, (fraction)
$S_{w\ max}$	Maximum water saturation, (fraction)
T	Temperature, (°C)
t	Time, (min.)
μ	Fluid viscosity, $ML^{-1}t^{-1}$, (cP)
V_{system}	Volume of system, (mL)
w_f	Fracture width, L, (cm)

TABLE OF CONTENTS

Page

LIST OF FIGURES

Page

LIST OF TABLES

Page

1. INTRODUCTION

1.1 Background

Darcy introduced the concept of permeability in 1856 by applying common mathematics of heat transfer that could be changed to describe fluid flow through porous rock. Permeability is a rock's capability to allow fluid passage through it. Darcy's Law is defined as the flow rate of fluid was linearly proportional to the cross-sectional area of the porous medium through which the fluid passes, as well as linearly proportional to the pressure differential divided by the inversely proportional to the fluid viscosity, and the length of the porous medium. The equation below defines permeability as the constant (k) that satisfies the equality of the relationship.

$$Q = -(kA)\left(\frac{\Delta P}{L}\right)\left(\frac{1}{\mu}\right) = -\frac{kA\Delta P}{\mu L} \quad \text{.....1-1}$$

While multiphase flow in porous media is discussed, the relative permeability (k_r) of a phase is a dimensionless ratio of effective permeability (k_e) of one phase and the absolute permeability (k) of the porous rock:

$$k_r = \frac{k_e}{k} \quad \text{.....1-2}$$

The sum of the relative permeabilities of each phase in a two-phase system will be less than or equal to one. If the sum of the relative permeabilities is less than one, this suggests there is flow interference between the phases. This indicates the relative permeability curve having a non-linear relationship regarding fluid saturations. Although relative permeability in a porous rock has been comprehensively studied, there is minimal published work investigating relative permeability in natural fractures for two-phase flow behavior through propped and unpropped fractures.

1.2 Literature Review

This section includes information on standard relative permeability measurements, the different procedures available for measurements, and the progression of the applications for measurement procedures to determine relative permeability behavior in natural fractures. The two methods that are generally applied for relative permeability measurements are the unsteady state method and steady-state method, which are supported by Abaci et al. (1992), Kantzas (2018), and Johnson et al. (1959). Detailed practices for relative permeability measurement methods have been analyzed and recorded by Romm (1966), Pieters & Graves (1994), Diomampo et al. (2001), and Pan et al. (1996).

1.2.1 Steady-State Relative Permeability

Steady-state tests vary from unsteady state tests by flowing brine and oil simultaneously through the test medium at a fixed ratio until there is no change in the measurements of pressure and outlet fractional flow rates with respect to time, as described by Kantzas (2018). Below is the detailed measurement procedure that was presented by Kantzas (2018) for the steady-state test and the calculation of the parameters required to produce the relative permeability curves.

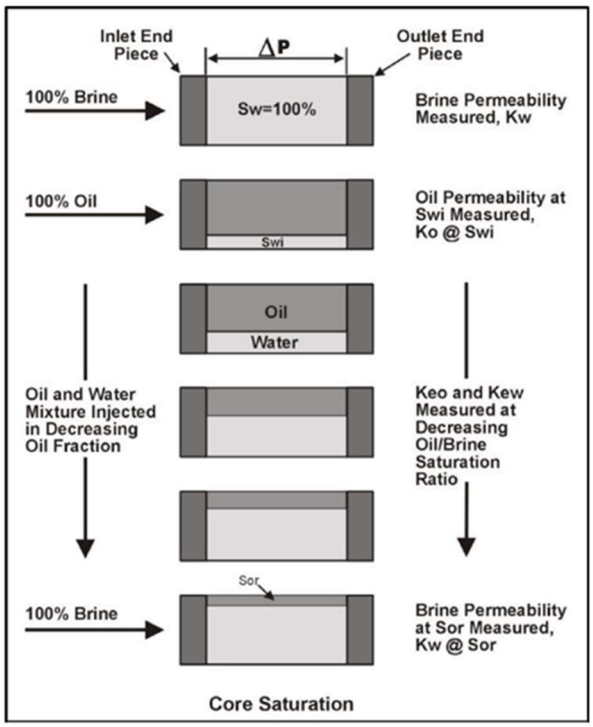

Figure 1-1 Steady-State Relative Permeability Waterflood Procedure Reproduced from Kantzas (2018).

As illustrated in Fig. 1-1, the steps to conduct a steady-state relative permeability test is as follows:

1. Condition fractured core in formation oil

2. Flood core with brine, measure the permeability of water at residual oil saturation.

3. Inject oil and flood down to irreducible water saturation at suitable differential pressure.

4. Measure the effective permeability of oil at irreducible water saturation.

5. Begin flowing oil and brine at fixed ratios until a constant differential pressure is obtained at each ratio.

6. Repeat step 5 with various oil/brine ratios (increasing water saturation).

7. Inject brine and flood down to residual oil saturation.

8. Calculate effective permeabilities using Darcy's Law.

Muskat et al. (1937) assumes that Darcy's Law is correct for each fluid, which shows that the volumetric flow for each respective phase can be represented by the equation below:

$$Q_i = \frac{k k_{ri} A \Delta P_i}{\mu_i L} \quad \text{.....1-3}$$

In this equation, (k) is the absolute permeability, (k_{ri}) is the oil or water relative permeability, (A) is the cross-sectional flow area, (ΔP_i) is the differential pressure, (L) is the length of the medium through which the flow is occurring, (μ_i) is the oil or water viscosity, and (Q_i) is the oil or water volumetric flow rate. Steady-state tests require the phase saturations to be calculated for each steady-state measurement. Phase saturations can be very difficult to estimate; nevertheless, numerous methods have proven to be successful for monitoring saturation during the steady-state experiments from Kantzas (2018). NMR Scanning, Gamma Attenuation Saturation Monitoring, CT Scanning, and X-Radiometry are methods that can be used to determine phase saturations. However, Steady-state tests have disadvantages such as the length of time required for each flow ratio to reach steady-state and the need to determine saturations utilizing advanced methods. Alternatively, the main advantage for the steady-state test is that a more complete relative permeability curve can be produced with measurements being viable across a broader range of saturations. Lastly, the steady-state analysis is acknowledged as the most accurate test available, and it can be applied to a variety of saturation ratios. Figure 1-2 shows steady state water-oil relative permeability example for an intermediate-wet core.

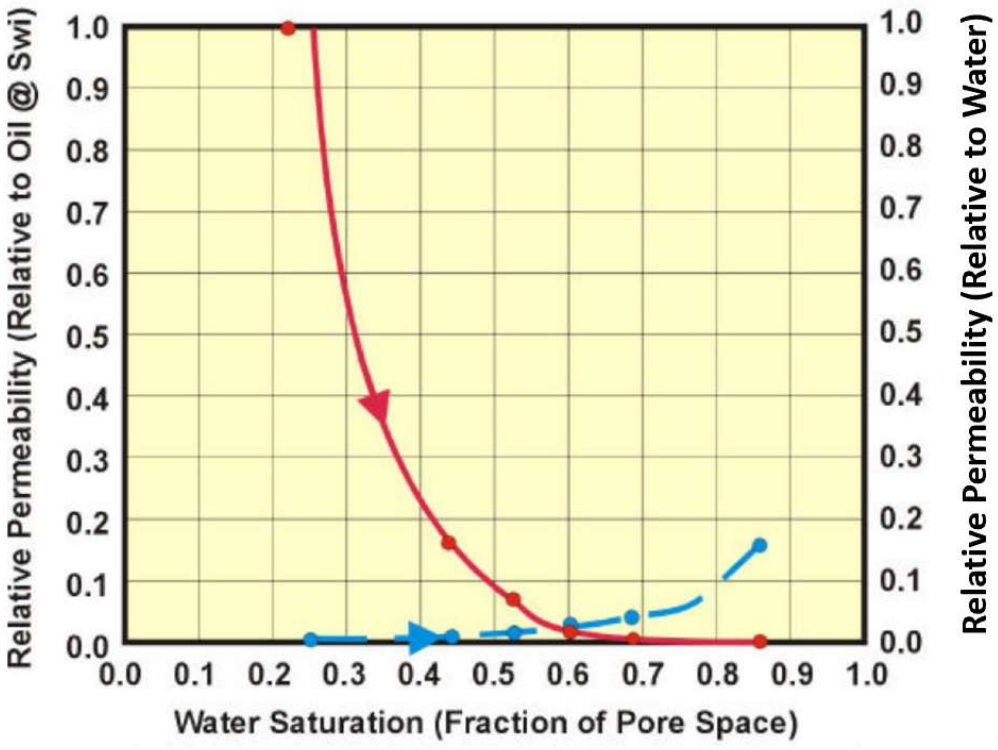

Figure 1-2 Steady-State Water-Oil Relative Permeability Example for an Intermediate-Wet Core Reproduced from Kantzas (2018).

1.2.2 Unsteady-State Relative Permeability

Unsteady state tests are conducted by measuring the relative permeability from displacing one phase by another. Below is the detailed measurement procedure that was presented by Kantzas (2018) for the unsteady state test and the calculation of the parameters required to produce the relative permeability curves.

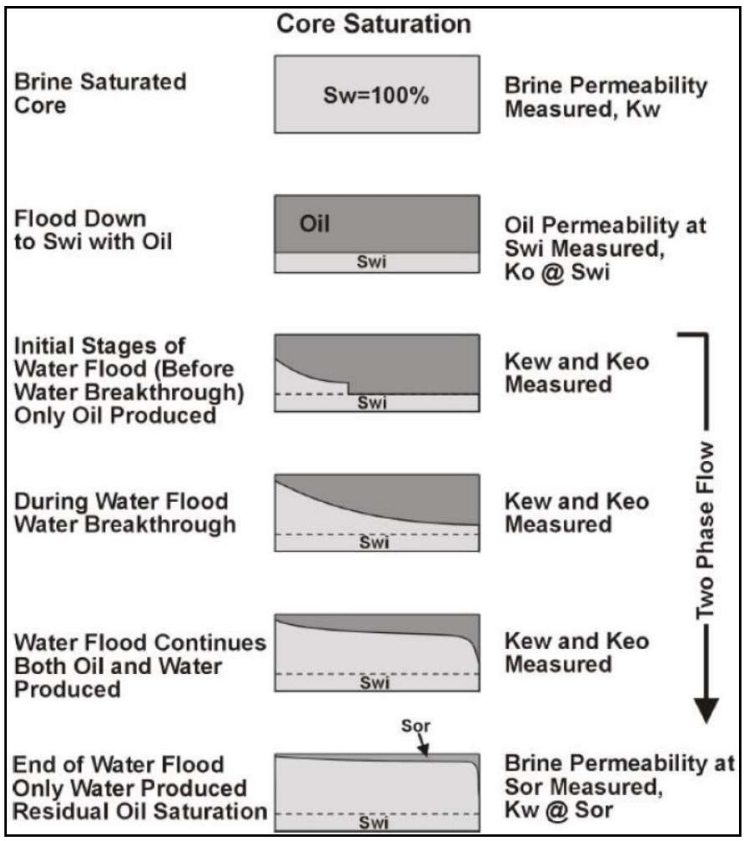

Figure 1-3 Unsteady State Relative Permeability Waterflood Procedure Reproduced from Kantzas (2018).

As illustrated in Fig. 1-3, the steps to conduct an unsteady-state relative permeability test is as follows:

1. Condition fractured core in formation oil.

2. Flood core with brine, measure the permeability of water at residual oil saturation.

3. Inject formation oil and flood down to irreducible water saturation at appropriate differential pressure.

4. Complete waterflood, measure differential pressure, incremental water production, and oil production.

5. Measure permeability of oil at irreducible water saturation.

6. Use the equations from Johnson, Bossler & Naumann (1959) analysis to calculate effective permeability of oil, effective permeability of water, the relative permeability of oil, and relative permeability of water for various water saturations.

7. Measure the effective permeability of water and calculate the relative permeability of oil at residual oil saturation.

When the test has been conducted, relative permeability calculations for this method are performed using the procedure known as the JBN analysis described by Johnson, Bossler, and Naumann, published by Johnson et al. (1959).

The required information for using the JBN analysis is recorded from the same procedure described in Kantzas (2018), which included differential pressure at initial conditions, differential pressure, the amount of displacing phase injected, the volume of water produced, the volume of oil produced, water viscosity, and oil viscosity. Three calculation stages are included in the JBN analysis.

Stage one is to establish the ratio of the relative permeability of oil to the relative permeability of water. The average water saturation must be plotted against the quantity of displacing fluid injected to determine this ratio. The inflection point shows the water breakthrough in this plot. The fractional flow at the core outlet is calculated using the equations below:

$$f_{o,out} = \frac{dS_{wav}}{dQ_i} \quad \text{.....1-4}$$

$$f_{o,out} = \frac{1}{1+\left(\frac{k_{rw}\mu_o}{k_{ro}\mu_w}\right)} \quad \text{.....1-5}$$

The ratio is solved using these two equations and all values known from the measured data during the test.

Stage two is to establish the relative permeability of oil. The ratio of the differential pressure to the pressure differential at initial conditions is plotted against the quantity of displacing phase injected. The injectivity ratio is calculated by using this plot; the equation for injectivity ratio is shown below:

$$I_R = \frac{\Delta P_i}{\Delta P}\frac{1}{Q_i} \quad \text{.....1-6}$$

A plot will be created using the equation above. Therefore, the relative permeability of oil can be calculated by using the equation below:

$$k_{ro} = f_{o.out}\frac{1}{\frac{d\left(\frac{1}{Q_i I_R}\right)}{d\left(\frac{1}{Q_i}\right)}} \quad \text{.....1-7}$$

Relative permeability of oil is determined in stage one, which results in the relative permeability of water to be calculated. Lastly, Welge (1952) presents a correction used to convert average saturations to outlet face saturations using the equation below:

$$S_{w.out} = S_{wav} - f_{o,out}Q_i \quad \text{.....1-8}$$

By plotting each phase's relative permeability as a function of the outlet face saturation, relative permeability curves can be graphed.

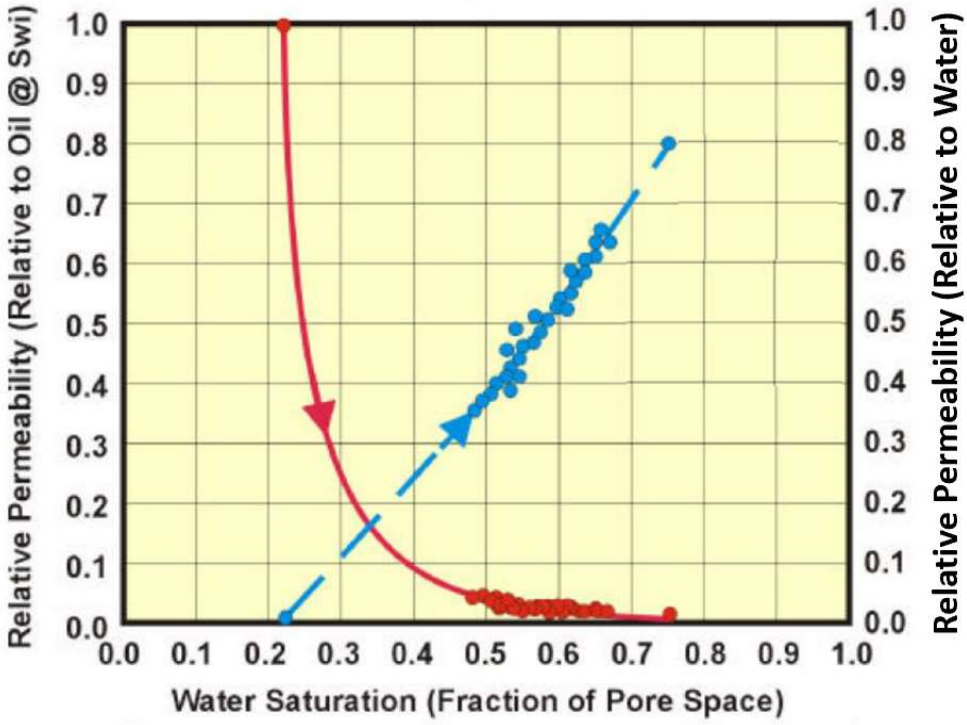

Figure 1-4 Unsteady State Oil-Water Relative Permeability Low Rate Flood Example for an Oil-Wet Core Reproduced from Kantzas (2018).

The unsteady state tests have some significant disadvantages, such as the need to estimate the average water saturation rather than measure it, which could result in significant errors and the inability to distinguish the shape of the relative permeability curve adequately. Although unsteady state tests have some significant disadvantages, it also has numerous advantages. Unsteady state test have the ability to obtain even saturation of each fluid present, it takes less time to conduct an unsteady state test than a steady-state test, and there is no need to scan the core to obtain in-situ saturations. Figure 1-4 shows an unsteady state oil-water relative permeability low rate flood example for an oil-wet core.

1.2.3 Relative Permeability Measurements in Fractures

Romm (1966) conducted experiments that were the first published laboratory examination of multiphase flow in a fracture. Romm performed this test by using artificial parallel-plate fractures to flow water and kerosene. The relative permeability of each phase was calculated. The results indicated a linear dependence of permeability on saturation.

Pieters and Graves (1994) duplicated Romm's experiment using the same fluids, but they used a high-resolution camera to record the fluid saturations behind a glass plate. They determined that there is a non-straight-line relative permeability behavior and emphasized the importance of accurately measuring the fluid saturations. Numerous studies are demonstrating the non-straight-line relative permeability behavior in fractures represented by parallel plates as described in work conducted by Diomampo et al. (2001), Pan et al. (1996), and Speyer et al. (2007). Other studies have attempted to measure fracture relative permeability. Still, these studies by Huo and Benson (2016) and Izadi et al. (2012) used synthetic fluids at room temperature and created the fracture using a saw cut. The most realistic study done to date used a 2” diameter core, with a generated fracture. Water and decane were used as the test fluids, and the test was conducted at room temperature. Sakurai et al. (2013) found a straight-line relationship at high fracture apertures and similar agreement to the Corey model at tiny apertures and high closure stress.

The significance of using reservoir fluids at reservoir conditions was defined by Mungan (1972). He exhibited the differences in relative permeability of a matrix between synthetic fluids and actual reservoir fluids. Numerous studies show analytically and simulation-derived models to estimate the relative permeability behavior in fractures as a function of fracture dimensions, surface roughness, and fluid properties. Petroleum engineers have widely accepted Romm's

linear relationship. It is still commonly used in the simulation of fractured reservoirs to this present day, as stated in publications by Gilman and Kazemi (1983) and Kasiri (2011).

1.3 Objective

The objective of this study is to experimentally measure the fracture relative permeability performance of the Eagle Ford core under typical reservoir temperature and actual fracture closure stress while utilizing real reservoir fluids such as formation brine, formation oil, and surfactant loaded fracturing fluid. The result of wettability modification and interfacial tension decrease in the resulting relative permeability of fractures is also studied. The main goal is to build a better understanding of oil-water flow within natural fractures within a reservoir.

2. EXPERIMENTAL DESIGN

2.1 Introduction

This section provides an overview of the core test samples, test fluids such as formation oil, reconstructed brine, and surfactants. The laboratory equipment and procedure used for the experimental measurements to calculate the oil-water relative permeability in fractures are also included. All tests were conducted using the steady-state relative permeability measurement method at typical Eagle Ford reservoir conditions such as reservoir temperature and closure stress.

2.2 Eagle Ford Shale Test Cores

Outcrop shale rock provided by Texas A&M University was used for all tests. The outcrop rock is from the Eagle Ford shale formation. The Eagle Ford shale was used to simulate reservoirs at a depth of 6000 feet (TVD). The rock was cored into four 1.5-inch diameter by 6 inches cores. Figure 2-1 shows a picture from Donovan et al. (2013) of the outcrop indicating where the Eagle Ford shale location is found.

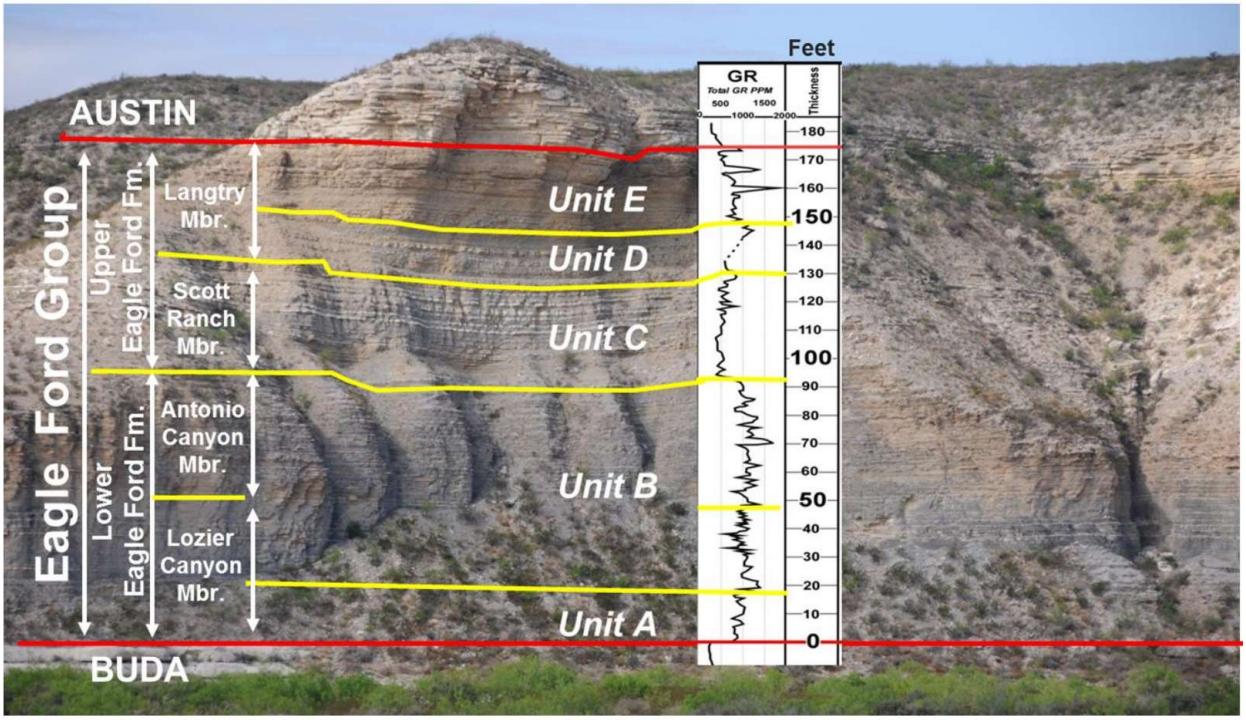

Figure 2-1 Outcrop Indicating Location of Eagle Ford Formation Reproduced from Donovan et al. (2013)

2.2.1 Core Mineralogy

The mineral content of each core was analyzed for each test sample. A small sample from each core was crushed, powdered, and sifted to a particle size less than 100 micrometers. The remains from the small sample were taken and scanned to have mineralogy for each core sample. A Bruker D8 Advance Eco XRD was used to scan the powdered remains. The mineralogy test results corresponding to each core sample are depicted in Table 2-1 and are shown graphically in Figure 2-2.

Table 2-1 X-Ray Diffraction Mineral Data for Eagle Ford Cores

X-Ray Diffraction Data				
Core Sample	1	2	3	4
Depth (ft.)	6000			
Calcite (%)	48.56	48.56	64.15	64.15
Quartz (%)	26.07	26.07	17.36	17.36
Dolomite (%)	5.23	5.23	5.02	5.02
Kaolinite (%)	8.65	8.65	4.79	4.79
Illite (%)	6.73	6.73	5.69	5.69
Pyrite (%)	3.71	3.71	0	0
Gypsum (%)	1.05	1.05	2.99	2.99
Total:	100	100	100	100

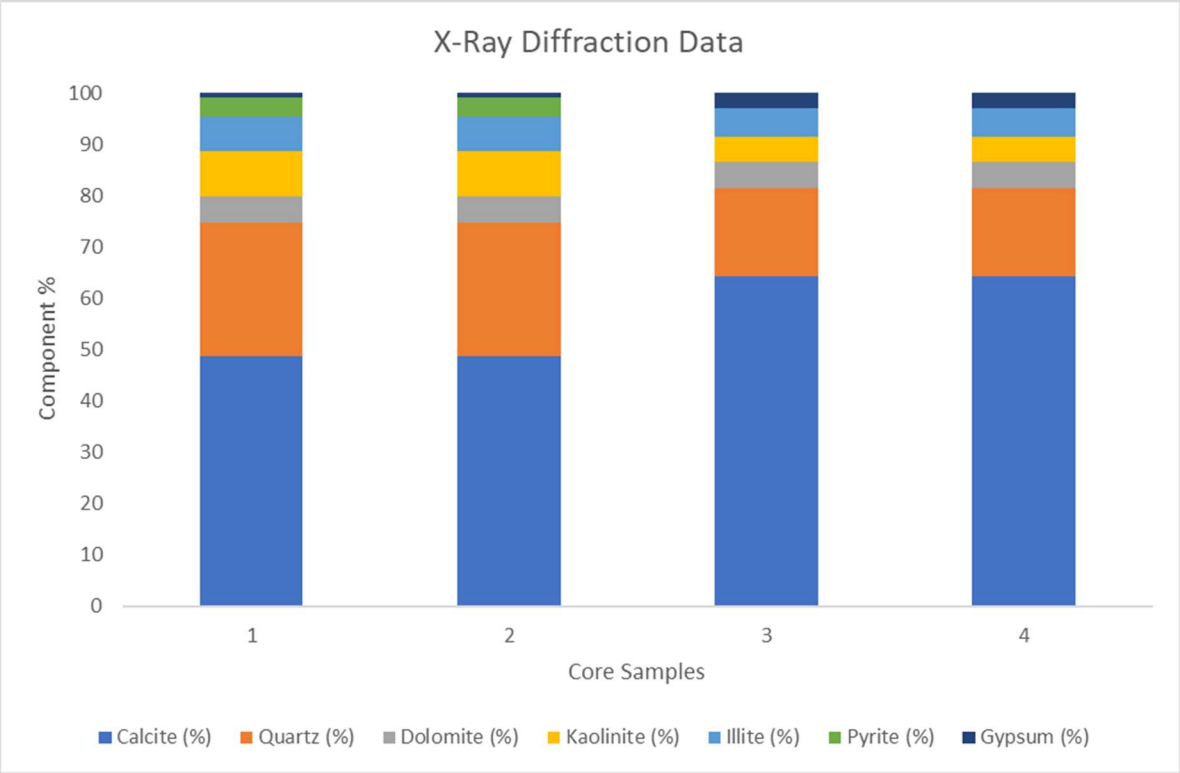

Figure 2-2 X-Ray Diffraction Mineral Data for Eagle Ford Cores

2.2.2 Core Preparation

The outcrop rock that was provided was approximately 9”x7”x7” rectangular chunks. Two lumps of outcrop rock were then cored into five test samples. Two 1.5” diameter x 6” length cores were used for oil-water relative permeability tests. Three 1.5” diameter x 2” length cores were used for contact angle measurements to determine the wettability. The two large core plugs were saw-cut to create an artificial fracture for the relative permeability test. Figure 2-3 shows a picture of one of the outcrop rocks used to core the test samples. Figure 2-4 shows the results and dimensions from coring the outcrop rock.

Figure 2-3 Outcrop Rock Used for Test Sample Coring

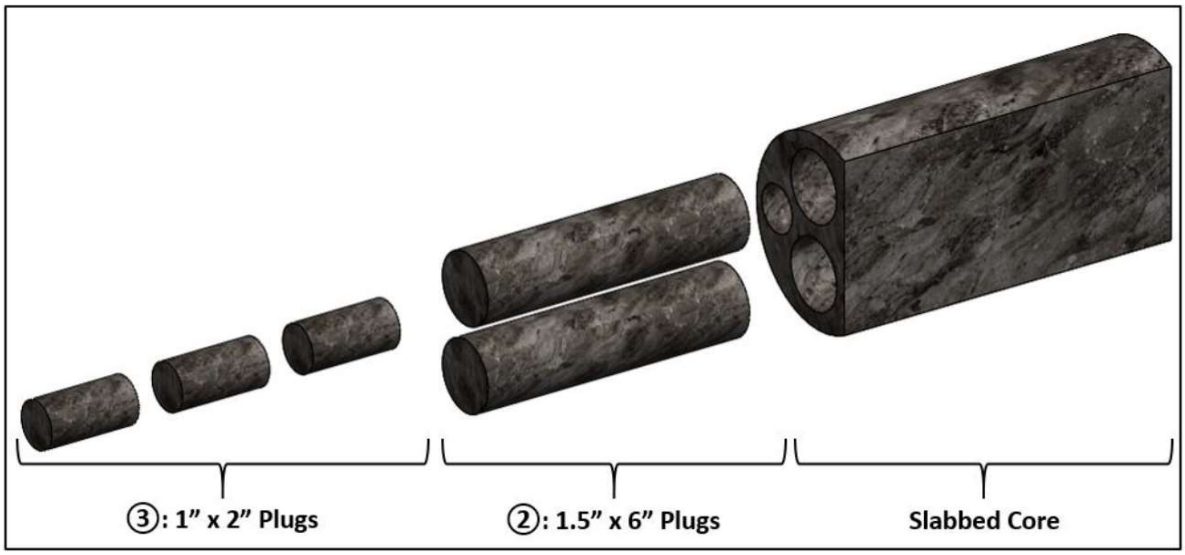

Figure 2-4 Drawing of Sample Test Specimen Cutting from Outcrop Section reproduced from Guerra (2017)

2.2.2.1 Saw-Cut Cores

Four (1.5" diameter x 6" length) cores were saw-cut using a 254μm thick diamond coated rotary blade. Each core sample had been cut along their longitudinal axis into equal halves. By saw cutting the core, it resulted in some surface roughness on the fracture faces. The resulting aperture from recombining the two halves was much smaller than anticipated to simulate a natural fracture. In order to combat this challenge, stainless steel shims were cut into 1/8" wide strips from 100μm thick shim stock. The two stainless steel shims were placed along the outer edges of the fracture parallel to the core's longitudinal axis to simulate a fracture aperture like that of a natural fracture. Figure 2-5 shows the placement of the shims along the edges of the fracture.

Figure 2-5 100µm Thick Stainless-Steel Shims to Control Fracture Aperture for Saw Cut Core

After the shims were cut to the appropriate size and positioned on one half of the core sample. Next, the other half was carefully positioned on top of the shims to match these pieces as close to perfect as possible. Then the pieces were reassembled with the stainless-steel shims in the middle; the core sample was then placed into a Viton® heat shrink sleeve. In order to keep the halves together during the experiments, the heat shrink sleeve confined these pieces by applying heat to the sleeve with a forced heat convection gun, which shrunk the sleeve around the core sample. Figure 2-6 shows the saw cut test sample within the Viton® heat shrink sleeve.

Figure 2-6 Saw Cut Core Wrapped in Viton® Heat Shrink Sleeve

After the sleeve was heat shrunk and allowed enough time to cool off, both faces of the sleeve were cut off the core to expose the entire core face to permit the full fracture aperture to be uncovered. Figure 2-7 shows the saw cut test sample within the Viton® heat shrink sleeve with the ends cut off.

Figure 2-7 Saw Cut Core Wrapped in Viton® Heat Shrink Sleeve with the Ends Trimmed Off

2.3 Fracturing Fluid Composition

The typical composition of fracturing fluid was used to test the oil-water relative permeability in fractures and was intended to represent a brine solution that could be implemented in the field. Surfactants were applied to the brine solution to produce four distinct compositions of fracking fluids for wettability alteration, which is frequently performed in the field. In the following paragraphs, the water salinity and the different surfactants used are evaluated.

2.3.1 Water Salinity

In order to test the oil-water relative permeability in natural fractures, the brine solution used was reconstructed to mimic a field brine composition as a fracking fluid that could be used. The composition that was used for this thesis was repeated from a test report used in a

dissertation from Guerra (2017). Guerra (2017) stated, "The total dissolved solids for the representative oilfield brine solution is 26,805.70 PPM. In order to reconstitute this brine solution, five main compounds were used: calcium chloride ($CaCl_2$), sodium chloride (NaCl), magnesium chloride ($MgCl_2$), sodium bicarbonate ($NaHCO_3$), and sodium sulfate (Na_2SO_4). The molecular weight of each ion within each corresponding compound was calculated, as shown in Table 2-2. Using the molecular weight of each ion by compound, the weight percent concentration of each ion by compound was calculated, as shown in Table 2-3. Using the weight percent ionic concentration by compound, the appropriate amount of each compound was calculated to result in the same ionic concentration as the target oilfield brine solution, with a final TDS of 26,810 PPM."

Table 2-2 Molecular Weight of Individual Ions by Compounds Used to Reconstitute Formation Brine Reproduced from Guerra (2017)

Frac Water Ionic Concentration		Molecular Weight by Compound				
Ion	g/L	$CaCl_2$ - g/mol	NaCl - g/mol	$MgCl_2$ - g/mol	$NaHCO_3$ - g/mol	Na_2SO_4 - g/mol
Calcium (as Ca)	0.481	40.078				
Magnesium (as Mg)	0.097			24.305		
Sodium (as Na)	9.704		22.990		22.990	45.980
Iron (as Fe)	0.016					
Chloride (as Cl)	15.995	70.900	35.450	70.900		
Sulfate (as SO_4)	0.363					96.056
Bicarbonate (as HCO_3)	0.150				61.016	
Total	26.806	110.978	58.440	95.205	84.006	142.036

Table 2-3 As Prepared Ionic Concentration of Reconstituted Formation Brine Reproduced from Guerra (2017)

Frac Water Ionic Concentration		Ionic Concentration by Compound					Reconstituted Concentration (g/L)
		$CaCl_2$ - (g/L)	NaCl - (g/L)	$MgCl_2$ - (g/L)	$NaHCO_3$ - (g/L)	Na_2SO_4 - (g/L)	
Ion	g/L	1.33	24.35	0.38	0.21	0.54	
Calcium (as Ca)	0.481	36.11%					0.480
Magnesium (as Mg)	0.097			25.53%			0.097
Sodium (as Na)	9.704		39.34%		27.37%	32.37%	9.811
Iron (as Fe)	0.016						0.000
Chloride (as Cl)	15.995	63.89%	60.66%	74.47%			15.904
Sulfate (as SO_4)	0.363					67.63%	0.365
Bicarbonate (as HCO_3)	0.150				72.63%		0.153
Total	26.806						**26.810**

2.3.2 Sample Conditioning and Surfactant Pairing

Four core samples 1.5” diameter x 6” length was saw-cut and prepared for testing. Next, the cores were conditioned in light Eagle Ford oil at a reservoir temperature of 270 °F for 60 days. For the cores to be conditioned properly, they need to be left soaking a minimum of 30 days. Table 2-4 shows the core samples with the corresponding aging dates.

Table 2-4 Summary of Sample Conditioning in Formation Oil

Sample Conditioning			
Sample Number	Start Date	End Date	Aging Time (Days)
1	11/22/2019	1/21/2020	60
2	11/22/2019	1/21/2020	60
3	12/5/2019	2/3/2020	60
4	12/5/2019	2/3/2020	60

Each core sample was then paired with one of the four fracturing fluids with or without surfactants. There were three different surfactants used in this thesis that is currently utilized in the field. The surfactant additives used were Surfactant A, Surfactant B, and Surfactant C for three of the core samples. Table 2-5 below shows the pairing of each fracturing fluid with their respective core sample.

Table 2-5 Core Sample Pairing with Respective Surfactant

Surfactant Pairing	
Sample Number	Surfactant Used
1	No Surfactant
2	Surfactant A
3	Surfactant B
4	Surfactant C

2.3.3 Surfactant Property Measurements

These four different fracturing fluids were used to measure the oil-water relative permeability in natural fractures. They contained the brine solution mentioned in section 2.3.1 and the addition of the surfactant additives discussed in section 2.3.2 at a concentration of one gallon per thousand gallons (1gpt). In order to determine the wettability variation provided by each surfactant additive, the contact angle (θ) of a single oil droplet surrounded by each fracturing fluid on a small surface chip from each core sample was measured at the reservoir temperature. Table 2-6 shows these four brine solutions were paired with corresponding core samples along with their surfactants and contact angles. Figure 2-8 shows the contact angle measurements graphically.

Table 2-6 Contact Angle Measurements for Each Surfactant

Contact Angle Measurements		
Sample Number	Surfactant Used	Contact Angle (°)
1	No Surfactant	110
2	Surfactant A	35.25
3	Surfactant B	34.67
4	Surfactant C	96.4

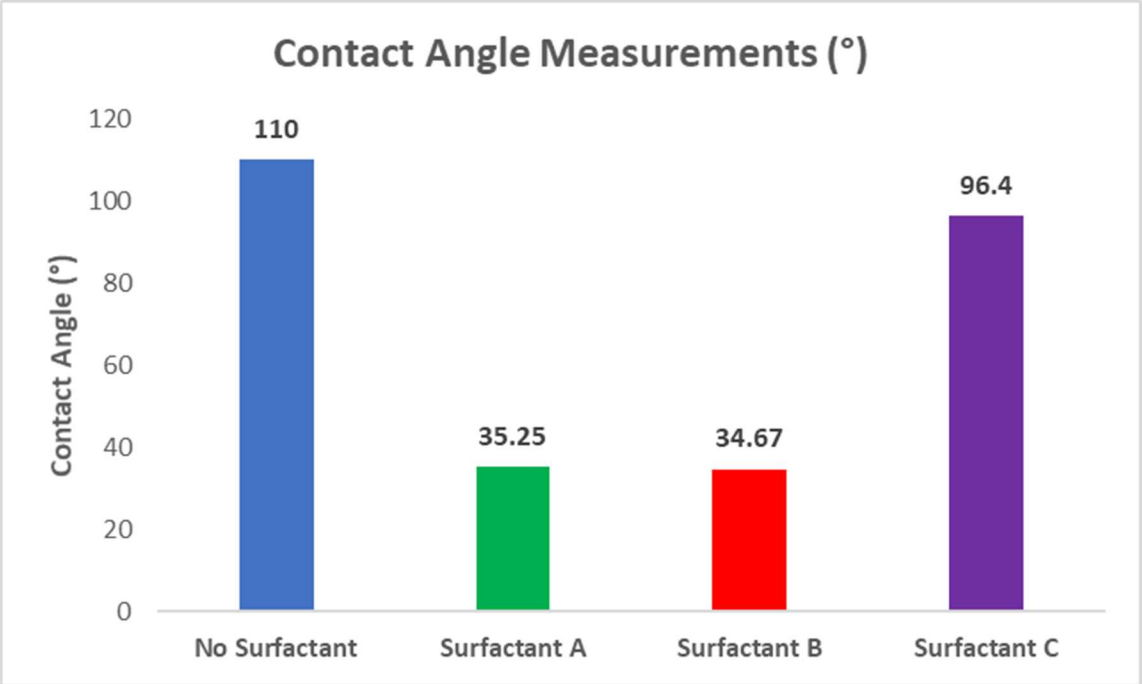

Figure 2-8 Contact Angle Measurements per Surfactant

The contact angle, which is measured for the fracturing fluid contacting the surface of the rock determines the wettability of the rock. The contact angles can be separated into three categories to describe surface wettability such as water-wet by having a contact angle of 0° to 75°, intermediate wet by having contact angle between 75°-105°, and oil-wet by having a contact angle greater than 105°. It can be seen by having just fracturing fluid with no surfactant that the contact angle shows the wettability of the core is slightly oil-wet. On the other hand, the fracturing fluid with surfactant changes the wettability from oil-wet to intermediate wet and water wet. Next, by using the formation oil and fracturing fluid with or without surfactant, the oil-water interfacial tension (σ) was measured using a capillary needle dispenser device at reservoir temperature. The analysis is conducted by dispensing a fixed volume oil droplet into the fracturing fluid and taking a high-resolution image. Next, this image is processed by drop-

shape-analysis software. The fracturing fluid and formation oil affect the interfacial tension measurements, not the rock sample. Table 2-7 shows the oil-water interfacial tension measurements for each different fracturing fluid. Figure 2-9 shows the interfacial tension measurements graphically.

Table 2-7 Interfacial Tension per Surfactant

Interfacial Tension Measurements (IFT)		
Sample Number	Surfactant Used	IFT (mN/m)
1	No Surfactant	21.78
2	Surfactant A	2.8033
3	Surfactant B	17.14
4	Surfactant C	14.3

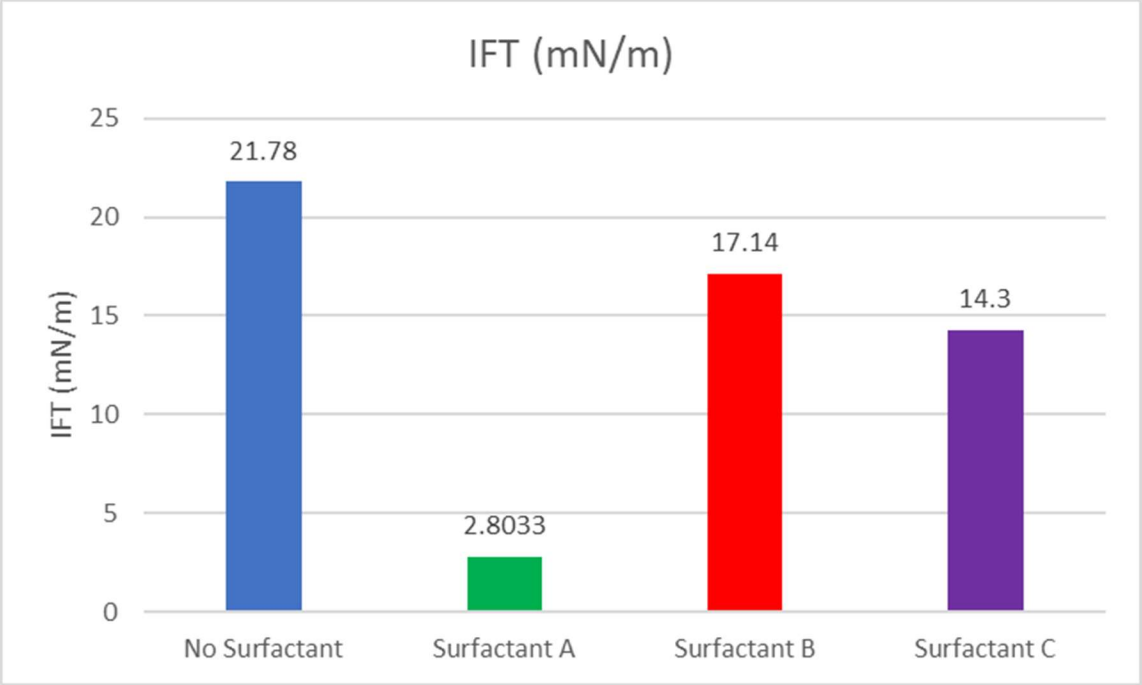

Figure 2-9 Interfacial Tension per Surfactant

Every surfactant additive caused changing degrees of wettability modification and reduced interfacial tension. The differences in pressure across the interface between the two phases are defined as capillary pressure. In order to calculate capillary pressure, the following equation was used:

$$P_c = \frac{2\sigma \cos\theta}{r}$$

The nomenclature for the equation above is defined as r is the pore radius, θ is the contact angle, and σ is the oil-water interfacial tension. For each fracturing fluid and core sample pairing, a capillary pressure value was calculated to describe the combined effect of both measured properties. Table 2-8 displays the calculated capillary pressure values for each core sample. Figure 2-10 shows the capillary pressure calculations graphically.

Table 2-8 Capillary Pressure per Surfactant

Capillary Pressure		
Sample Number	Surfactant Used	Pc (mN/m/r)
1	No Surfactant	-14.90
2	Surfactant A	4.58
3	Surfactant B	28.19
4	Surfactant C	-3.19

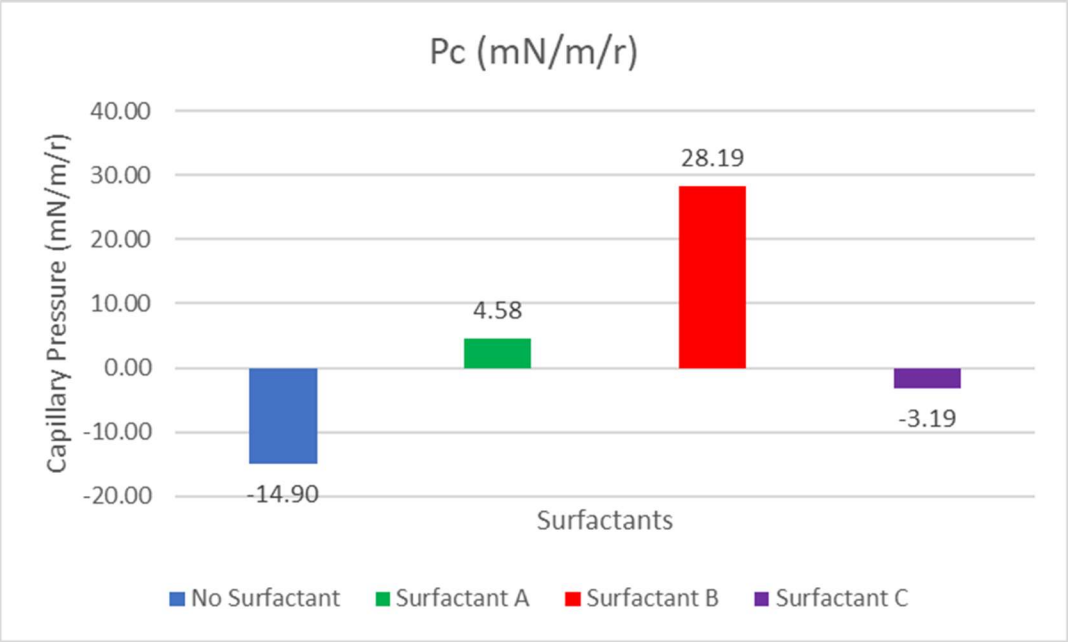

Figure 2-10 Capillary Pressure per Surfactant

2.4 Experimental Equipment

The following experimental setup was designed only for oil-water relative permeability tests for natural fractures. The experimental setup includes many components such as two syringe pumps, confining pressure hydraulic hand pump, hassler type core holder, micro Coriolis flowmeter, temperature controller, inlet pressure transducer, outlet pressure transducer, and confining pressure transducer. Figure 2-11 shows a schematic of the experimental apparatus and the functions of each component. Figure 2-12 is a picture of the experimental laboratory setup.

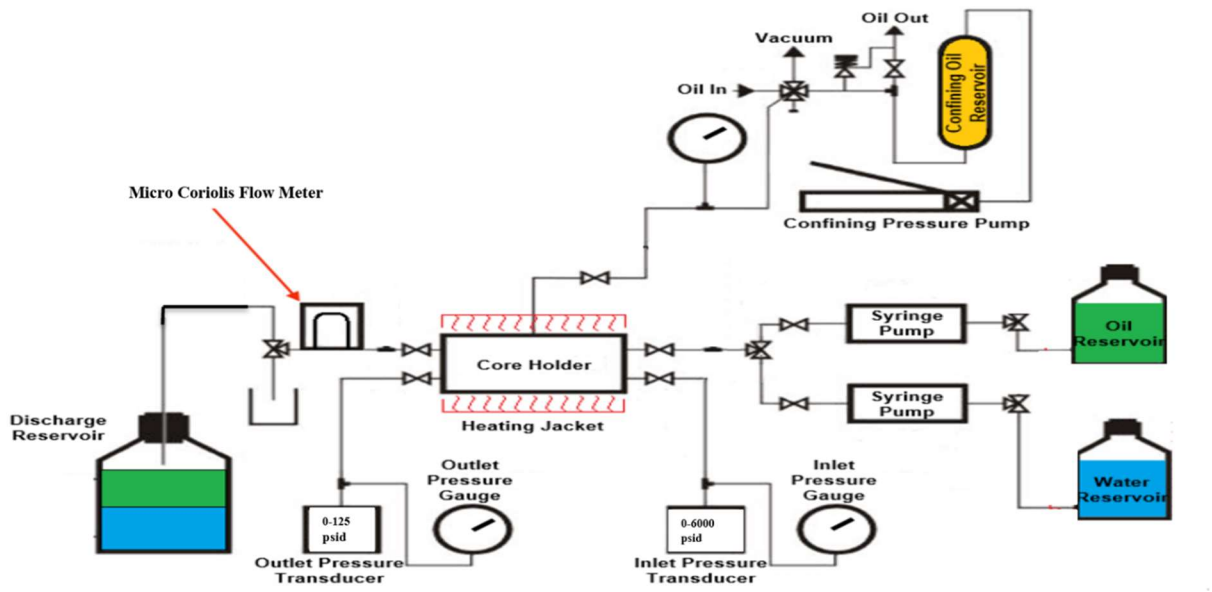

Figure 2-11 Schematic of Experimental Equipment Set-up for Relative Permeability Test modified from Guerra (2017)

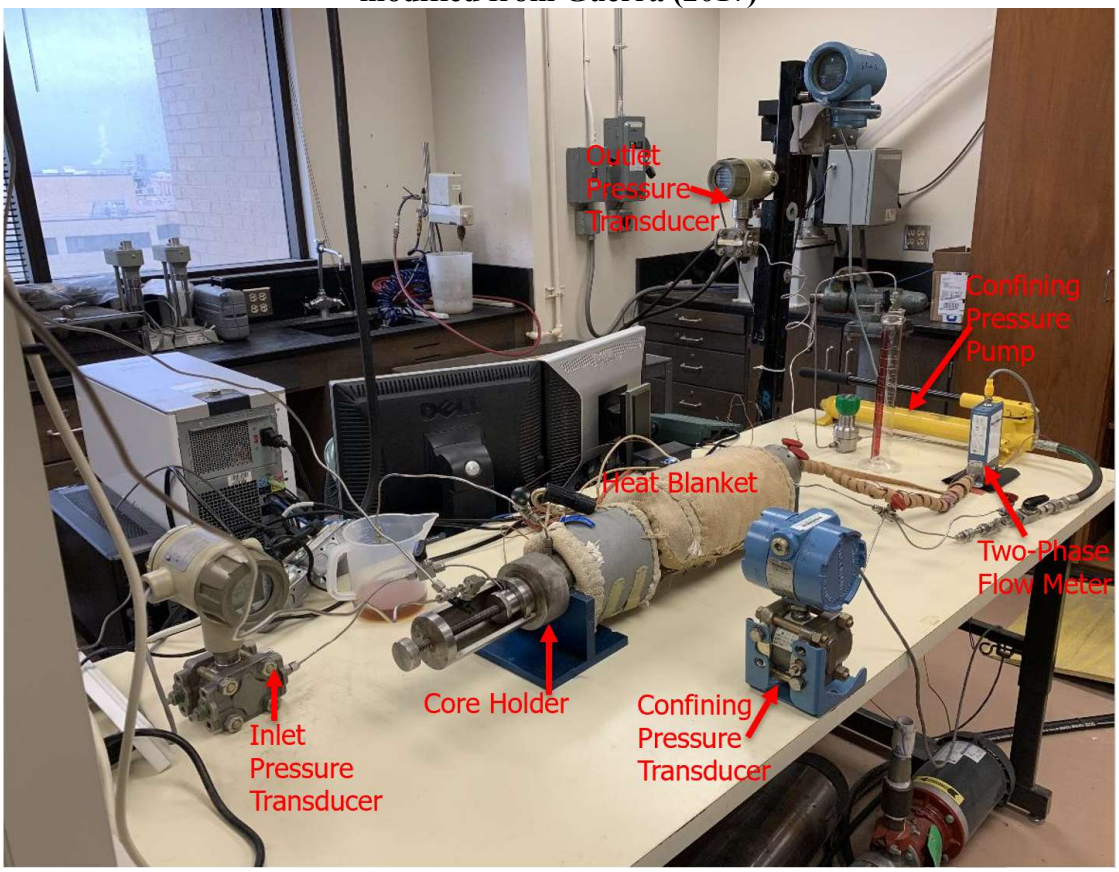

Figure 2-12 Experimental Equipment Set-up for Relative Permeability Test

2.4.1 Syringe Pumps

The syringe pumps used were Teledyne ISCO Model 500D that has a capacity of 507 mL and a pressure rating of 3750 psig. The two syringe pumps were used to control the injection rates of the fluids, one for oil and the other for the fracturing fluid. In order to control the injection rates of each fluid simultaneously, a Teledyne ISCO D-Series Pump controller was utilized. Figure 2-13 shows the two syringe pumps, one for fracturing fluid on the left and the other for formation oil on the right, along with the pump controller.

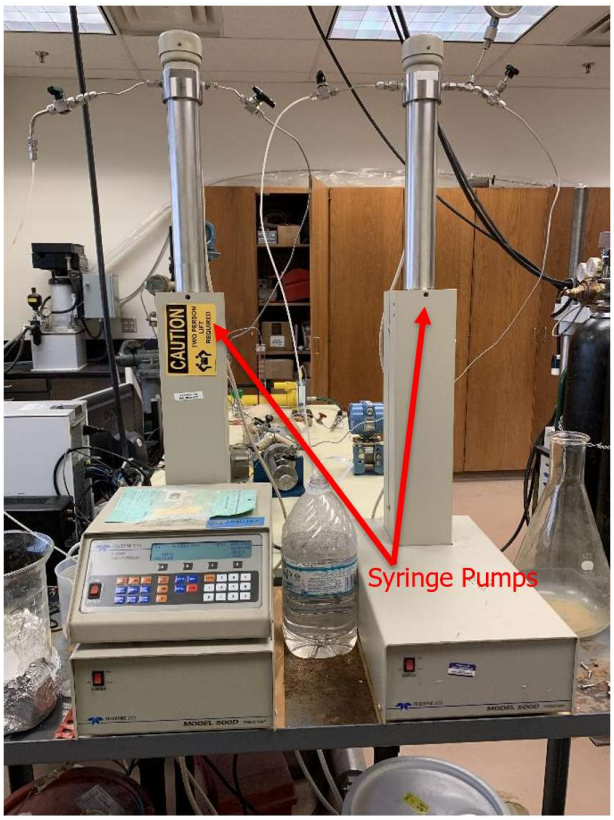

Figure 2-13 Teledyne ISCO 500D Syringe Pumps and Teledyne ISCO D-Series Pump Controller

2.4.2 Confining Pressure Hydraulic Hand Pump

An Enerpac P39 hydraulic hand pump was used, which has a working pressure of up to 10,000 psig. In order to simulate reservoir closure stress on the core, this pump was needed to apply the appropriate amount of confining pressure to the core holder to achieve the reservoir closure stress for the relative permeability test. Figure 2-14 displays the Enerpac P39 pump utilized.

Figure 2-14 Enerpac P39 Hydraulic Hand Pump Utilized for Confining Pressure

2.4.3 Hassler Type Core Holder

A Phoenix Instruments Model TAM-HAS-1.5X20-3K-10 Hassler type core holder was used to provide the reservoir closure stress. The operating pressure and temperature limits for this core holder are 3,000 psi and 300 °F, respectively. The core holder can house cores up to 20-inches in length with 1.5-inches diameter. This core holder was manufactured from 17-4PH stainless steel with the moistened parts made from Hastelloy to prevent corrosion. Figure 2-15 shows the core holder covered with a heating blanket around the main body and two insulating jackets.

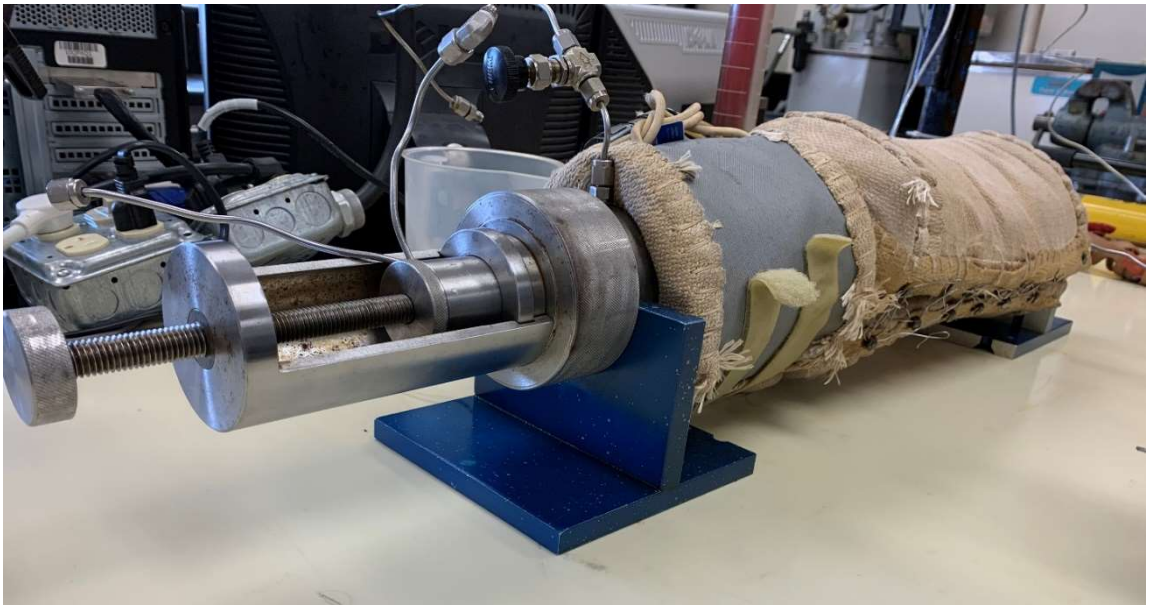

Figure 2-15 Hassler Type Core Holder with Heating Blanket and Insulating Jacket Attached.

Figure 2-16 shows the assembled core holder with the heating blanket attached and the insulating jackets removed in order to view the main components.

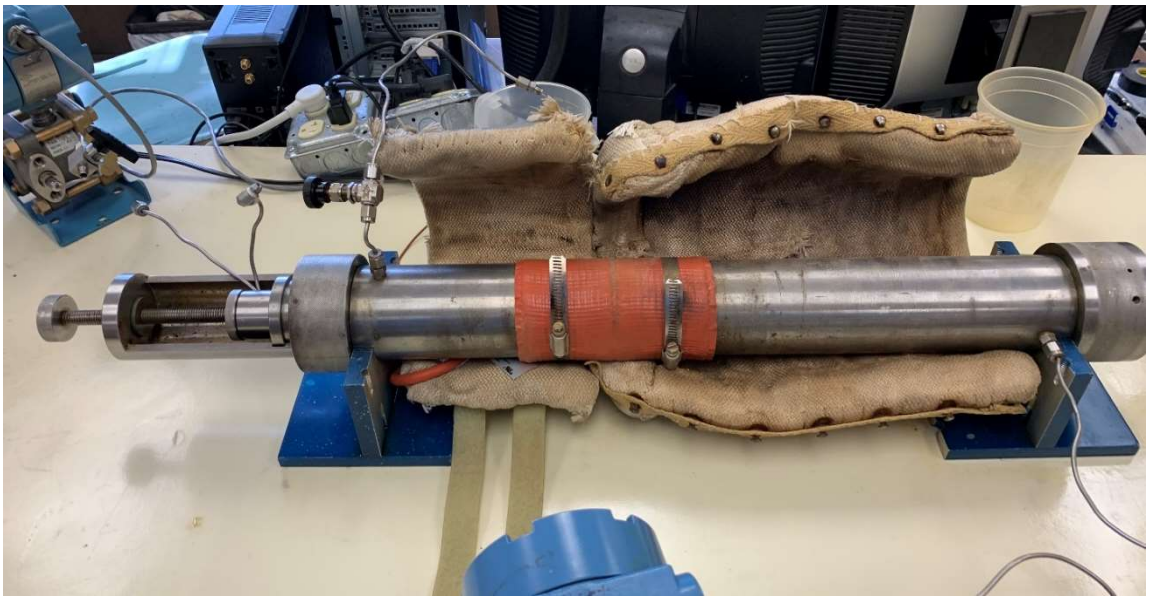

Figure 2-16 Hassler Type Core Holder with Heating Blanket Attached and Insulating Jackets Removed

Figure 2-17 shows the core holder disassembled showing the inlet piston piece, saw cut core sample, and outlet piston piece that is housed inside the core holder during the experiment.

Figure 2-17 Hassler Type Core Holder Disassembled Showing Inlet Piston Piece, Saw-Cut Core Sample, and Outlet Piston Piece

Figure 2-18 shows a close-up picture of a saw cut core not used in the experiments held in between the inlet and outlet pistons with the heat shrink unattached to show the simulated fracture.

Figure 2-18 Close-up of Saw Cut Core Sample Between Inlet and Outlet Pistons

Both the piston faces of inlet and outlet have miniature channels cut concentric to the circumference as well as channels cut in the radial direction to permit flow distribution over the whole face of the core sample. Figure 2-19 shows a close-up picture of the inlet piston face along with the edge of the fractured core sample.

Figure 2-19 Close-up of Saw Cut Core Sample and Inlet Piston Face with Two Channels

2.4.4 Micro Coriolis Flow Meter

The Micro Coriolis flowmeter used was a Micro Motion Model LF2M sensor. The outlet piston was connected to this ultra-low flow rate mass flow and density meter. The density range is 0 – 2 g/cm^3, with a density measurement accuracy of ±0.005 g/cm^3. The mass flow rate range for this sensor is 0.2 – 5 g/min, with a mass flow measurement accuracy of ±1% of the maximum rate. Figure 2-20 shows a picture of the Micro Motion Model LF2M sensor that was used. Figures 2-21 and 2-22 show the calibration curves for both mass flow rate and density measurements, respectively.

Figure 2-20 Micro Motion Model LF2M Flow Meter

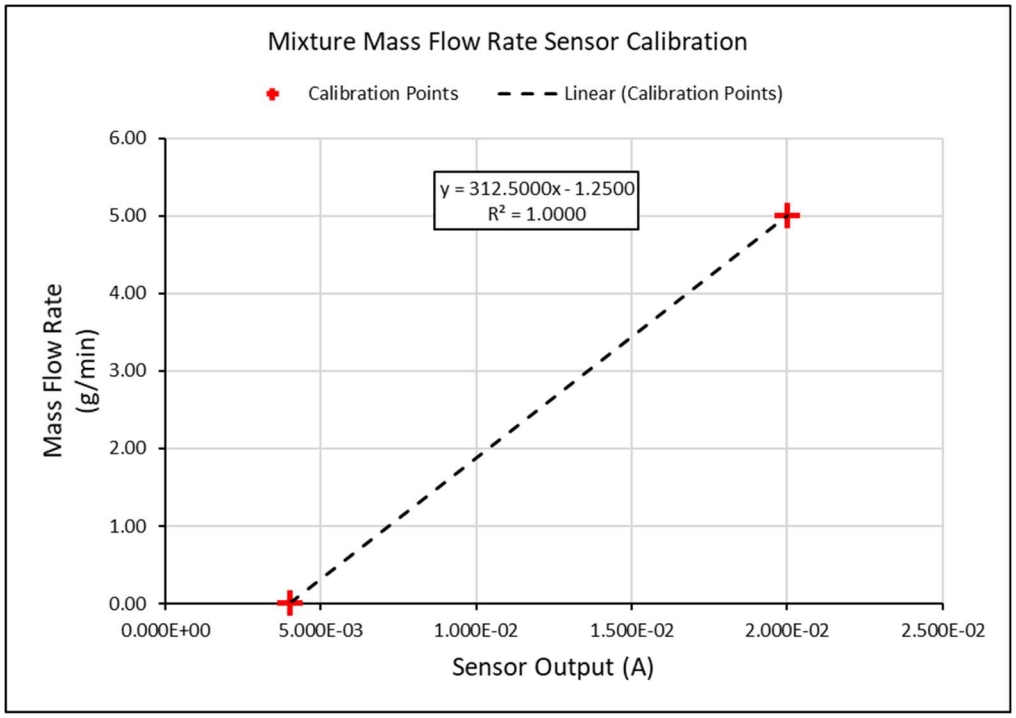

Figure 2-21 Mass Flow Rate Sensor Calibration Curve

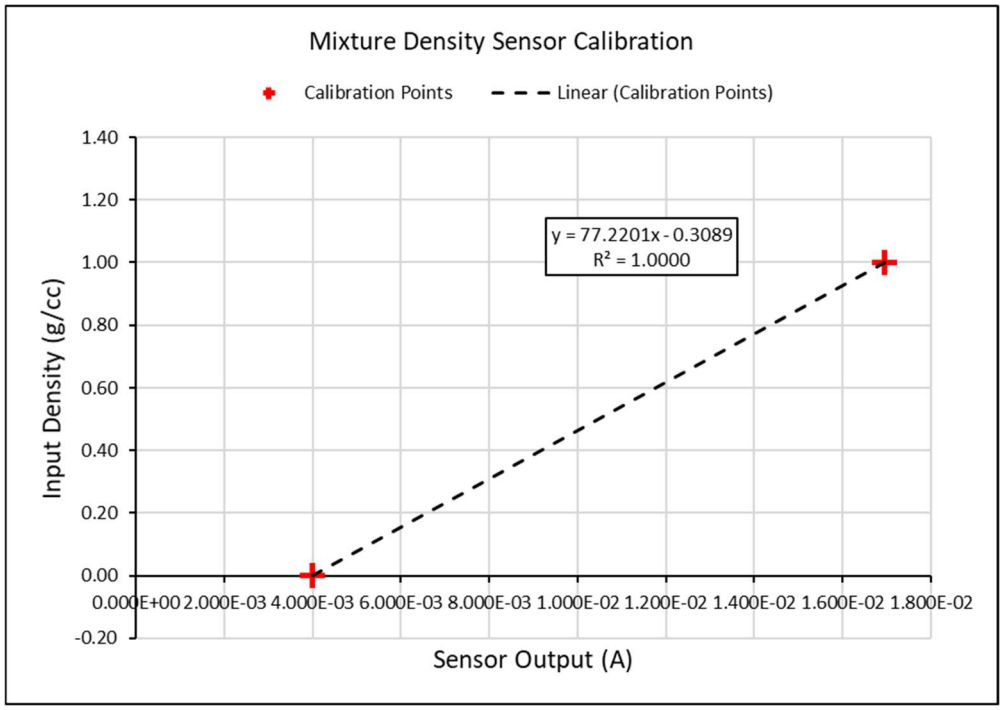

Figure 2-22 Density Sensor Calibration Curve

2.4.5 Temperature Controller

An Omega CN7500 PID temperature controller controlled the heating blanket. This temperature controller uses a type J thermocouple attached in between the core holder's outer body and the heating blanket. The operator determines a set point, and the controller uses a proportional-integral-derivative controller to adjust power input to the heating blanket to reach and keep the desired temperature. In order to determine the actual temperature of the test sample inside the core holder, the core holder was temporarily assembled with a saw cut sample with a type J thermocouple placed at the center of the test sample in between both fracture halves. Then, the heating blanket was set at various temperatures in order to determine the appropriate set point to reach the desired reservoir temperature inside the core holder. For the case of this thesis, the desired reservoir temperature was 270 °F. Each heating trial began at room temperature and was recorded for 16 hours. After conducting multiple trials, it was determined that the required set point temperature needed for this experiment was 310 °F, which results in steady-state core temperature of 270 °F. Figure 2-23 shows a picture of the Omega CN7500 PID heat controller used for testing. Figure 2-24 shows an image of the heating calibration curve used to determine reservoir temperature.

Figure 2-23 Omega CN7500 PID Temperature Controller

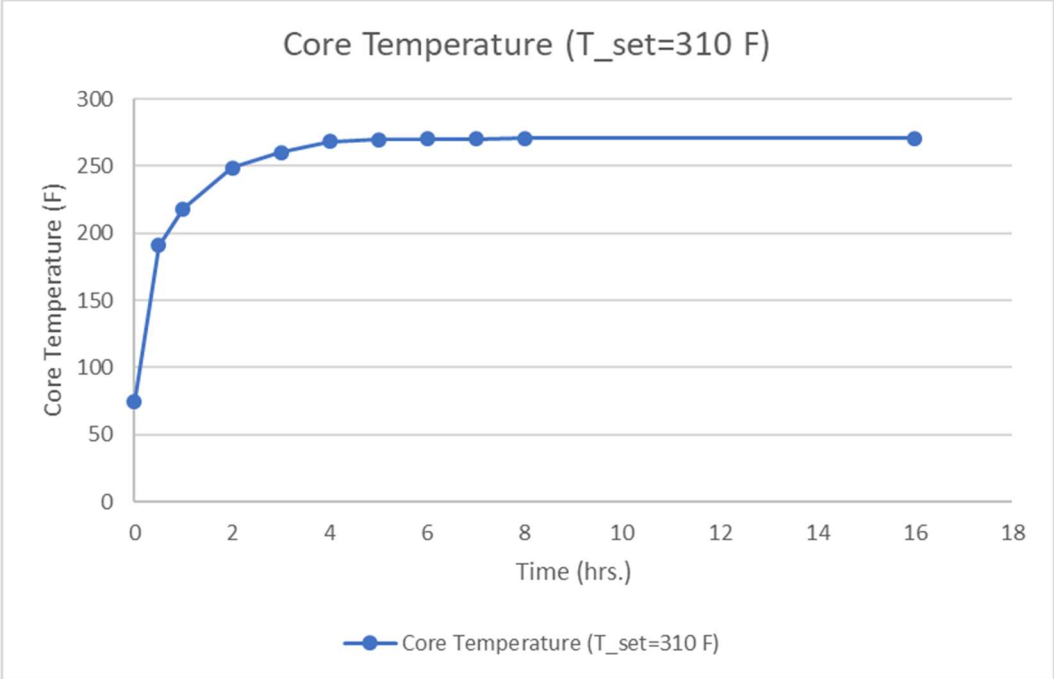

Figure 2-24 Transient Core Temperature Heating Curve

2.4.6 Inlet Pressure Transducer

The inlet pressure was monitored and recorded using a Rosemount Alpha-line Pressure Transducer and had a maximum working pressure of 6000 psig. Using a dead weight tester, the digital output signal generated from the inlet pressure transducer was calibrated to convert the milliamp output to a pressure value. Figure 2-25 shows a picture of the dead weight tester used to calibrate all transducers used in this experimental setup. Figure 2-26 shows the calibration curve for the inlet pressure transducer.

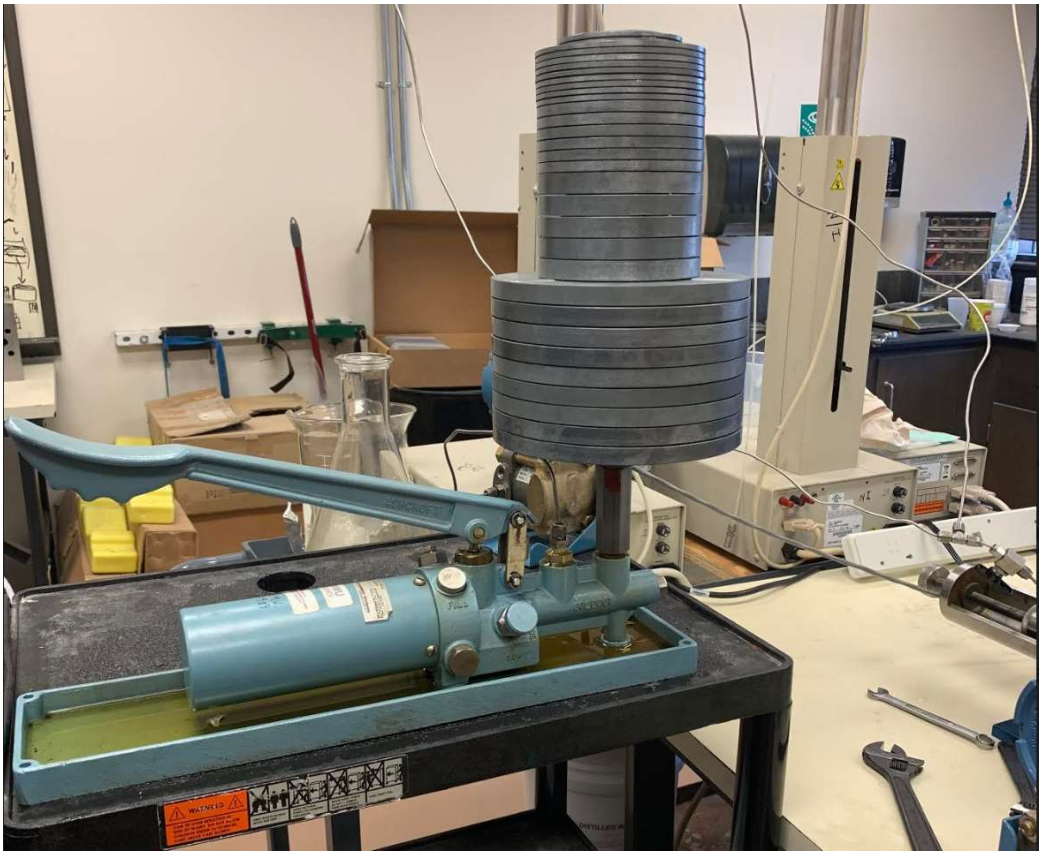

Figure 2-25 Dead Weight Tester Used to Calibrate Pressure Transducer

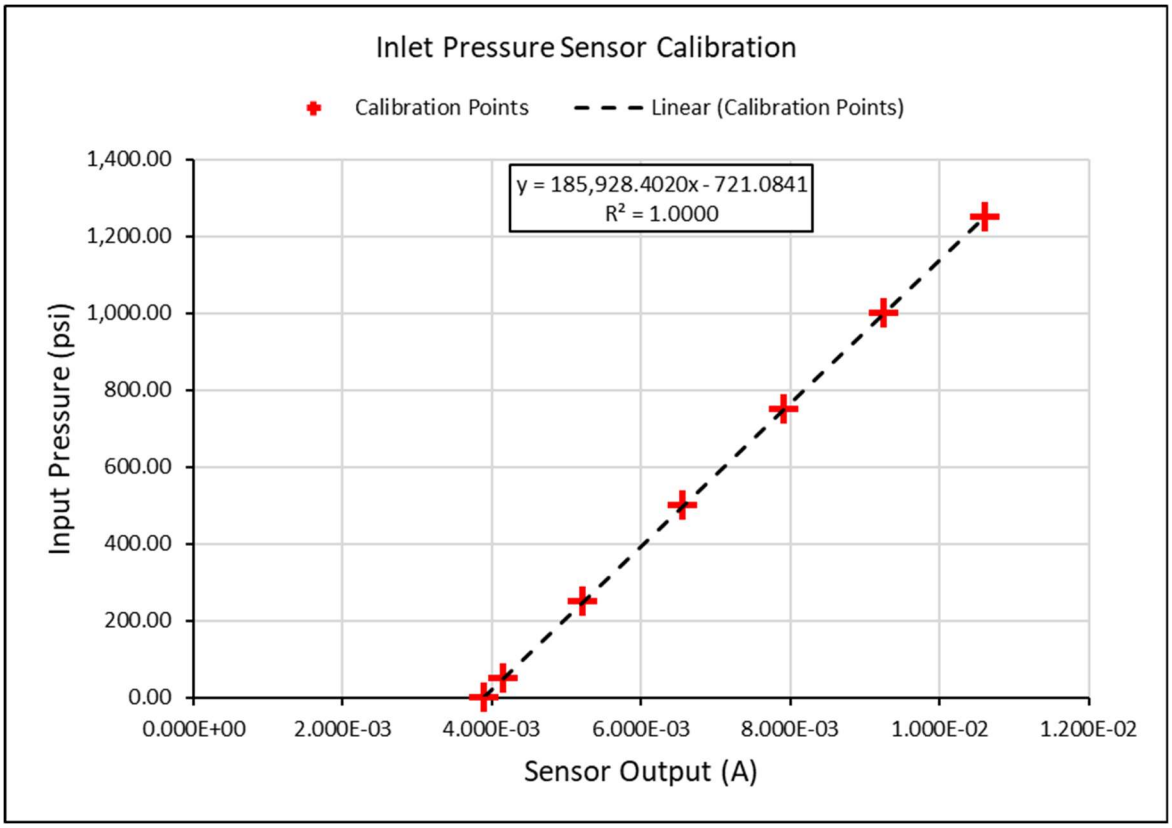

Figure 2-26 Inlet Pressure Sensor Calibration Curve

2.4.7 Outlet Pressure Transducer

The outlet pressure was monitored and recorded using a Rosemount Alpha-line Pressure Transducer and had a maximum working pressure of 125 psig. Using a dead weight tester, the digital output signal generated from the outlet pressure transducer was calibrated to convert the milliamp output to a pressure value. Figure 2-27 shows the calibration curve for the outlet pressure transducer.

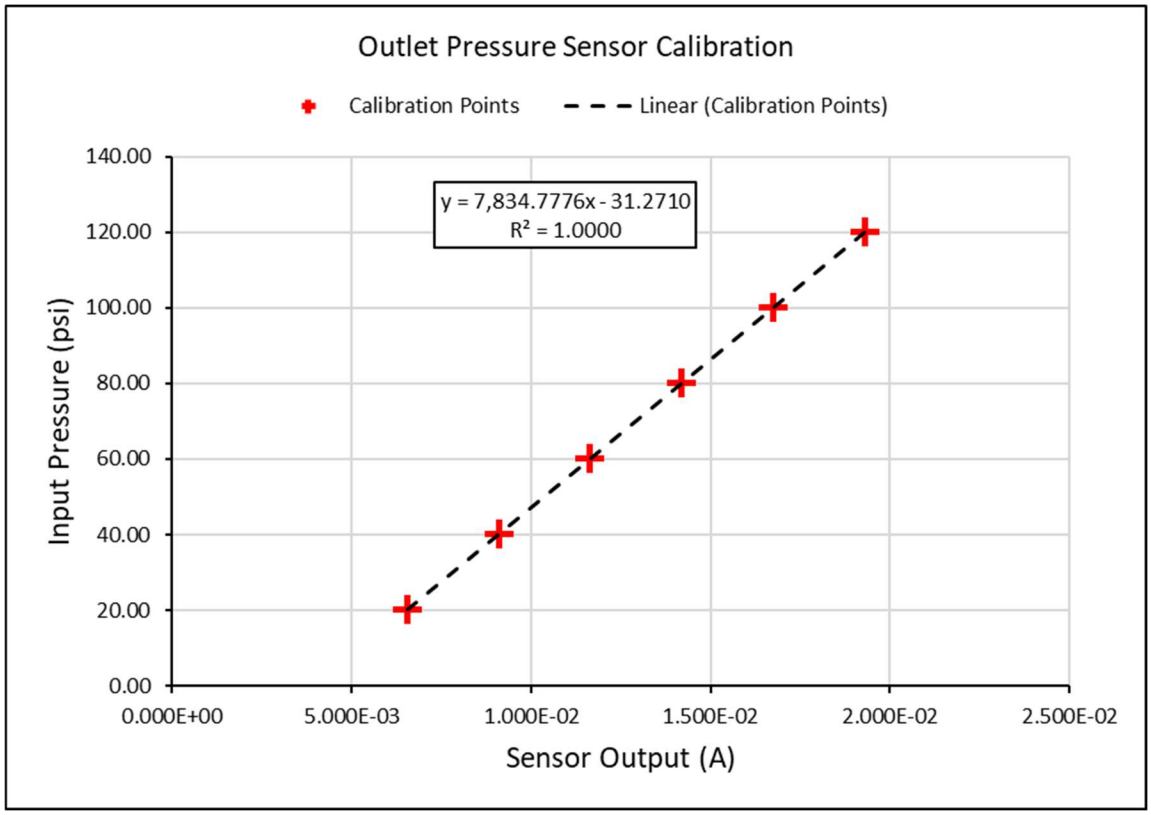

Figure 2-27 Outlet Pressure Sensor Calibration Curve

2.4.8 Confining Pressure Transducer

The confining pressure was monitored and recorded using a Rosemount Alpha-line Pressure Transducer and had a maximum working pressure of 6000 psig. Using a dead weight tester, the digital output signal generated from the confining pressure transducer was calibrated to convert the milliamp output to a pressure value. Figure 2-28 shows the calibration curve for the confining pressure transducer.

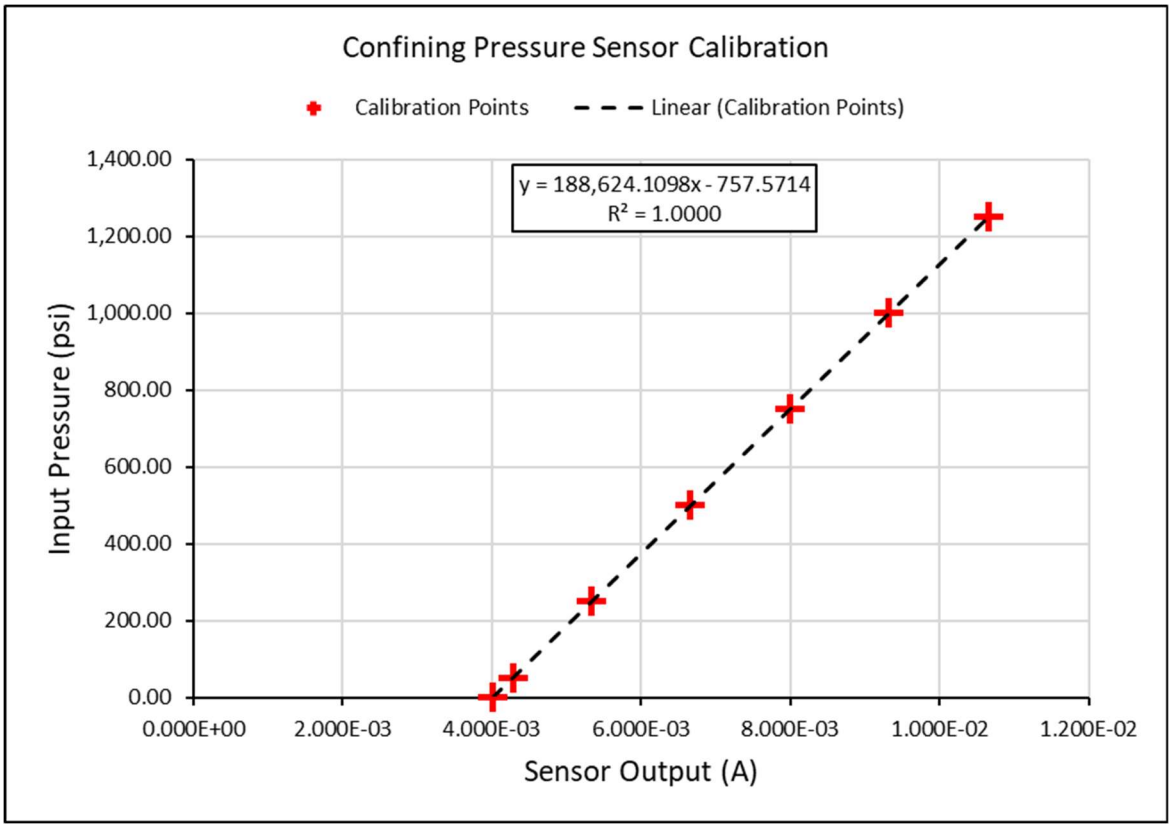

Figure 2-28 Confining Pressure Sensor Calibration Curve

2.4.9 Digital Oil Bath

In order to condition all saw-cut core samples in Eagle Ford oil, a LABNICS Equipment LOB – 100T Digital Oil Bath was used. The oil bath has a maximum heating temperature of 280°F. Figure 2-29 shows the oil bath used to soak all saw cut core samples, and Figure 2-30 shows the cages used to soak the test samples in Eagle Ford oil.

Figure 2-29 LABNICS Equipment LOB – 100T Digital Oil Bath

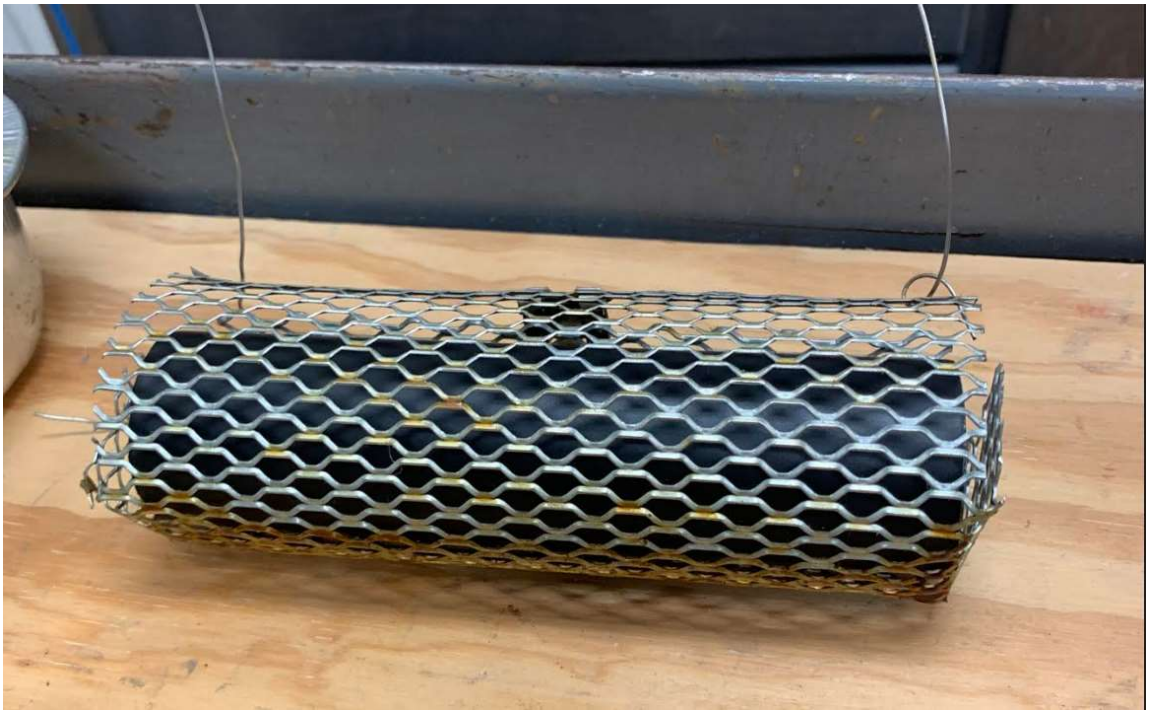

Figure 2-30 Cages for Core Conditioning

2.5 Experimental Procedure

After preparing the core samples, the core samples were conditioned in Eagle Ford oil for 60 days at a reservoir temperature of 270°F. When the core sample is conditioned, the core is then placed within the core holder. Next, a steady-state oil-water relative permeability test is ready to be performed.

The experimental setup procedure used for all tests conducted is as follows:

1. Insert outlet piston into core holder.
2. Insert the saw-cut core sample into the core holder from the inlet end, aligning the fracture in a horizontal orientation.
3. Insert inlet piston and attach inlet connector with the screw to secure inlet piston and hand tighten the piston to confirm proper mating of piston and core faces.
4. Fill both pumps A & B with fracturing fluid and formation oil, respectively.
5. Connect inlet and outlet pressure lines, double-check connections to ensure proper torque has been applied.
6. Fasten heating blanket and insulating jackets on core holder.
7. Set heating blanket temperature on the controller to target temperature 310 °F.
8. Allow at the least 6 hours for the core holder and core to reach the target temperature and reservoir temperature 270 °F.
9. After reservoir temperature has been reached, close the confining pressure relief valve and apply desired confining stress 2800 psig and allow confining pressure to stabilize. Adjust if necessary.
10. Finally, the core sample and core holder are properly prepared and ready to begin the oil-water relative permeability measurement procedure.

When the setup procedure was finished, the core samples tested had seven measurement steps that were used. Table 2-9 shows the measurement procedure that was utilized.

Table 2-9 Steady-State Relative Permeability Measurement Procedure Summary

Steady State Relative Permeability Test Procedure						
Step	Procedure	Measured Value		End Point	Oil Injection Rate (mL/min.)	Water Injection Rate (mL/min.)
1	Flood core with oil, measure k_o @S_w=0	k_o			1	0
2	Inject oil and water (F_w=20%)	k_{eo}	k_{ew}		0.8	0.2
3	Inject oil and water (F_w=40%)	k_{eo}	k_{ew}		0.6	0.4
4	Inject oil and water (F_w=60%)	k_{eo}	k_{ew}		0.4	0.6
5	Inject oil and water (F_w=80%)	k_{eo}	k_{ew}		0.2	0.8
6	Flood core with water, measure k_{ew} @S_{or}		k_{ew} @ S_{or}	S_{or}	0	1
7	Flood core with oil, measure k_o @S_{wirr}	k_{eo} @S_{wirr}		S_{wirr}	1	0

Table 2-10 shows an example pump schedule used for all testing. Each test stage for this example was allowed 70 minutes to reach steady state. A total of 280 mL of oil and 210 mL of water was used in this test.

Table 2-10 Steady-State Relative Permeability Pump Schedule

Steady State Fracture Relative Permeability Test Pump Schedule										
Test Stage	Start Time (HH:MM:SS)	$F_{w\text{-injected}}$	End Point Saturations	End Point Rel Perms	Oil (mL/min)	Water (mL/min)	Elapsed Time (min)	Interval Time (min)	Cumulative Oil (mL)	Cumulative Water (mL)
Stage 1	9:14:00 AM	0.0		k_o	1.00	0.00	70	70	70	0
Stage 2	10:24:00 AM	0.2			0.80	0.20	140	70	126	14
Stage 3	11:34:00 AM	0.4			0.60	0.40	210	70	168	42
Stage 4	12:44:00 PM	0.6			0.40	0.60	280	70	196	84
Stage 5	1:54:00 PM	0.8			0.20	0.80	350	70	210	140
Stage 6	3:04:00 PM	1.0	S_{or}	$k_{rw\text{-}Sor}$	0.00	1.00	420	70	210	210
Stage 7	4:14:00 PM	0.0	S_{wirr}	$K_{ro\text{-}Swirr}$	1.00	0.00	490	70	280	210
End Time	5:24:00 PM							Total Volur	280	210
Total Time	8:10	hrs:mins								

2.6 Steady-State Oil-Water Relative Permeability Determination

Two sets of data are recorded during the experiment; one set includes the data from all sensors, such as mixture mass flow rate ($\dot{m}_m$) and mixture density (ρ_m) from the Coriolis mass flow and density meter. The inlet and outlet pressure are logged to acquire the differential

pressure (ΔP). The confining pressure ($P_{confining}$) is the piece of data recorded from the data acquisition board. The other set of recorded data includes the syringe pump data that verifies the water injection rate ($Q_{w,\,in}$) and oil injection rate ($Q_{o,\,in}$). All data was logged in one second time intervals throughout the experiment. For each stage, steady-state is reached when there are no change phase saturations ($Q_{x,\,in} = Q_{x,\,out}$) and no change in differential pressure (ΔP_{ss}).

By using the Coriolis mass flow and density meter, the mixture volumetric flow rate is then calculated as follows:

$$Q_{m,out} = \frac{\dot{m}_m}{\rho_m} \quad \text{.....2-1}$$

$$\rho_m = \frac{\rho_o Q_{o,out} + \rho_w Q_{w,out}}{Q_{m,out}} \quad \text{.....2-2}$$

The outlet volumetric flow rate for each phase can be calculated using equations 2-3 and 2-4.

$$Q_{w,out} = \left(\frac{\rho_m - \rho_o}{\rho_w - \rho_o}\right)\left(Q_{m,out}\right) \quad \text{.....2-3}$$

$$Q_{o,out} = Q_{m,out} - Q_{w,out} \quad \text{.....2-4}$$

By using Darcy's Law in equation 2-5, the absolute permeability of the fracture is calculated during the first stage of the experiment by flooding the core with 100% saturation of oil.

$$k = -\frac{Q\mu L}{A\Delta P_{ss}} \quad \text{.....2-5}$$

Equations 2-6 and 2-7 represent the equations used to calculate the effective permeabilities of each phase at fixed fractions through the fracture.

$$k_{eo} = -\frac{Q_o \mu_o L}{A_o \Delta P_{ss}} \quad \text{.....2-6}$$

$$k_{ew} = -\frac{Q_w \mu_w L}{A_w \Delta P_{ss}} \quad \text{.....2-7}$$

Equations 2-8 and 2-9 represent the equations used to calculate the relative permeability of each phase.

$$k_{ro} = \frac{k_{eo}}{k} \quad \text{……...……..……...…2-8}$$

$$k_{rw} = \frac{k_{ew}}{k} \quad \text{……...……..……...…2-9}$$

Lastly, equations 2-10 and 2-11 represent the equations used to calculate the oil and water saturations in the fracture at each stage.

$$S_o = \frac{(\sum Q_{o,in}t - \sum Q_{o,out}t)}{V_{system}} \quad \text{……...……..……...…2-10}$$

$$S_w = \frac{(\sum Q_{w,in}t - \sum Q_{w,out}t)}{V_{system}} \quad \text{……...……..……...…2-11}$$

A steady-state relative permeability curve is produced by plotting the water relative permeability and oil relative permeability as a function of the water saturation. Additionally, a check for laminar flow is performed to confirm the legitimacy of Darcy's law for the purpose of the oil-water relative permeability.

When dealing with non-circular tubes or channels, a term commonly used is the hydraulic diameter (D_h) inflow problems defined by White (2011). The problem can be simplified as flow through parallel plates when analyzing flow through fractures, which can be defined as flow through rectangular channels. Equation 2-12 shows the formula used to determine the hydraulic diameter for rectangular channels.

$$D_h = \frac{4A}{P_{we}} \quad \text{……...……...…2-12}$$

where P_{wet} is the wetted perimeter in contact with the fluid, and A is the cross-sectional area. Equation 2-13 defines hydraulic diameter when the flow through parallel plates is separated by an aperture height (h_f) and has a width (w_f).

$$D_h = \frac{4h_f w_f}{2(h_f + w_f)} \quad \text{.....2-13}$$

Equation 2-14 defines the simplified hydraulic diameter by taking the limit as the width tends to infinity when the width of the fracture is much greater than the aperture height ($w_f \gg h_f$).

$$D_h = \lim_{w_f \to \infty} \frac{4h_f w_f}{2(h_f + 2w_f)} = 2h_f \quad \text{.....2-14}$$

According to White (2011), equation 2-15 defines how to calculate Reynold's Number for fully developed flow in parallel plates having an aperture height (h_f).

$$R_e = \frac{\rho v \ _h}{\mu} \quad \text{.....2-15}$$

All experiments were carried out using a total volumetric flow rate of 1mL/min, which led to a Reynolds Number of 3.25 and 0.63 for water and oil, respectively, which validates Darcy's Law for all test completed by indicating laminar flow (R_e<1000).

3. FRACTURE OIL WATER RELATIVE PERMEABILITY TEST RESULTS

3.1 Introduction

This section contains the results from all eight steady-state oil-water relative permeability experiments, which are grouped into five sets. The first set of data contains a graph in which the differential pressure (ΔP), confining pressure ($P_{confining}$), mixture density (ρ_m), and volumetric flow rate of water (Q_{iw}) and oil (Q_{io}) are plotted. All data was recorded at one second intervals and was plotted as a moving average at hundred second intervals.

The second set of data shows a table summarizing the recorded measurements from the previous Figure once steady state was reached for each stage. The inlet and outlet pressure are recorded as well as the mass flow rate, density, and differential pressure for each stage.

The third set of data presents a table summarizing the calculated values, such as effective permeabilities of water and oil and relative permeabilities for water and oil. The calculated water saturations as well are included along with the fractions of oil and water injected.

The fourth set of data displays the resulting oil-water relative permeability curve for each test. The curve is plotted as a function of calculated water saturation along with a best fit generalized Brooks-Corey relationship. The last set contains graphs displaying the comparisons of each test based on the surfactant type. This graph will display the contrast of oil-water relative permeability curves for each test run for that specific surfactant.

3.2 Generalized Brooks-Corey Relations for Oil-Water Relative Permeability

The original Brooks-Corey correlation for relative permeability published by Brooks and Corey (1966) was modified to the generalized Brooks-Corey relation allowing its use for a broader range of rock wettability traits. By applying the generalized correlations for an oil-water

system, the curvature can be adjusted to allow the best fit for experimental data, and it follows a power-law relationship. Lastly, it can also be used to change the endpoints of each respective relative permeability curve.

Below are the two equations used to fit the experimental data to the generalized Brooks-Corey relation:

$$k_{ro} = k_{ro(S_{w\,min})}\left[\frac{S_{w\,max}-S_w-S_{or}}{S_{w\,max}-S_{wi}-Sor}\right]^{C_o} \quad \text{.....3-1}$$

$$k_{rw} = k_{rw(S_{or})}\left[\frac{S_w-S_{wirr}}{S_{w\,max}-S_{wirr}-Sor}\right]^{C_w} \quad \text{.....3-2}$$

where the endpoint relative permeability for oil is $k_{ro\,(Sw\,min),}$ and water is $k_{rw\,(Sor)}$. S_{wi} is the initial water saturation, $S_{w\,max}$ is the maximum water saturation, S_{w}irr is the irreducible water saturation, and S_{or} is the residual oil saturation. The Corey water exponent C_w, and Corey oil exponent C_o each range in value from 1 to 6 and control the curvature of each curve. Lastly, k_{ro} and k_{rw} are the relative permeabilities to oil and water, respectively.

3.3 Test Results

A total of eight different experiments were conducted, where no surfactant, surfactant A, surfactant B, and surfactant C were all tested twice. Figure 3-1 shows the recorded data for the first test conducted with no surfactant, and Table 3-1 summarizes the data measured. Table 3-2 displays a summary of the calculated relative permeabilities, and Figure 3-2 presents the relative permeability curve produced.

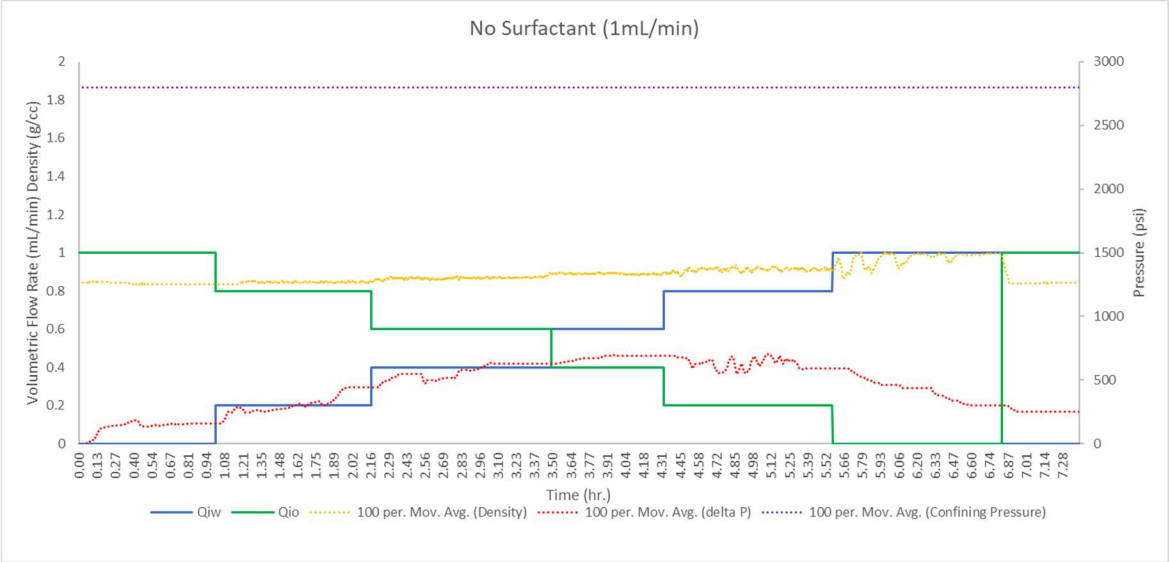

Figure 3-1 Recorded Data from Fracture Relative Permeability Test 1 for No-Surfactant

Table 3-1 Measured Fracture Relative Permeability Test 1 Data for No-Surfactant

MEASURED / READ						
$Q_{w\text{-}in}$ (mL/min)	$Q_{o\text{-}in}$ (mL/min)	P_{in} (psi)	P_{out} (psi)	ΔP (psi)	$M_{m\text{-}out}$ (g/min)	$\rho_{m\text{-}out}$ (g/mL)
0.00	1.00	164	12	152	0.8	0.80
0.20	0.80	455	12	443	0.84	0.84
0.40	0.60	640	11	629	0.88	0.88
0.60	0.40	700	10	690	0.92	0.92
0.80	0.20	598	8	590	0.96	0.96
1.00	0.00	310	6	304	1	1.00
0.00	1.00	263	11	252	0.8	0.80

Table 3-2 Calculated Fracture Relative Permeability Test 1 Data for No- Surfactant

Calculated						
Fo	Fw	Sw	Keo (md)	Kew(md)	Kro	Krw
1	0	0.00	652.55	0.00	1.00	0.00
1	0	0.1	393.60	0.00	0.60	0.00
0.8	0.2	0.32	179.12	37.32	0.27	0.06
0.6	0.4	0.41	94.61	52.56	0.14	0.08
0.4	0.6	0.52	57.50	71.87	0.09	0.11
0.2	0.8	0.6	33.62	112.07	0.05	0.17
0	1	0.81	0.00	271.89	0.00	0.42

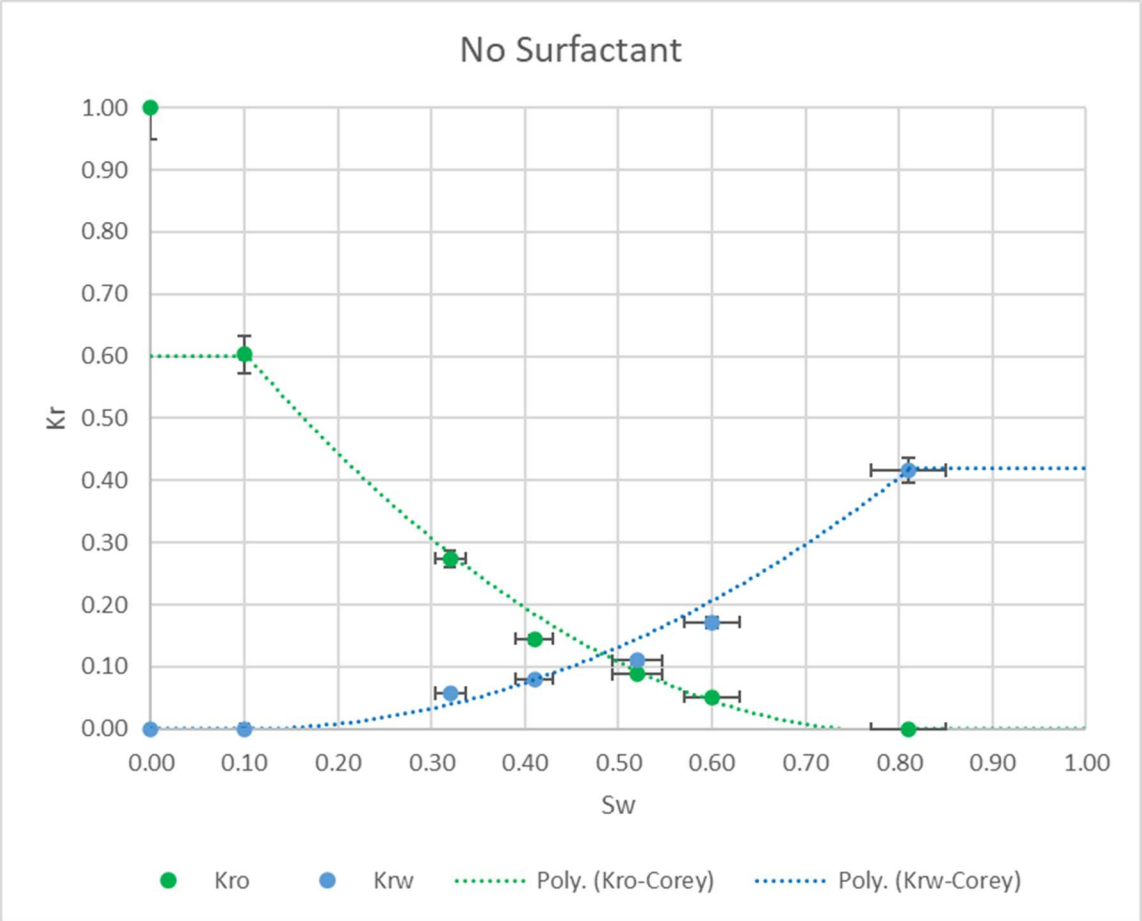

Figure 3-2 Calculated Fracture Relative Permeability Curve and Corey Fit for Test 1 No-Surfactant

Figure 3-3 shows the recorded data for the second test conducted with no surfactant, and Table 3-3 summarizes the data measured. Table 3-4 displays a summary of the calculated relative permeabilities, and Figure 3-4 presents the relative permeability curve produced.

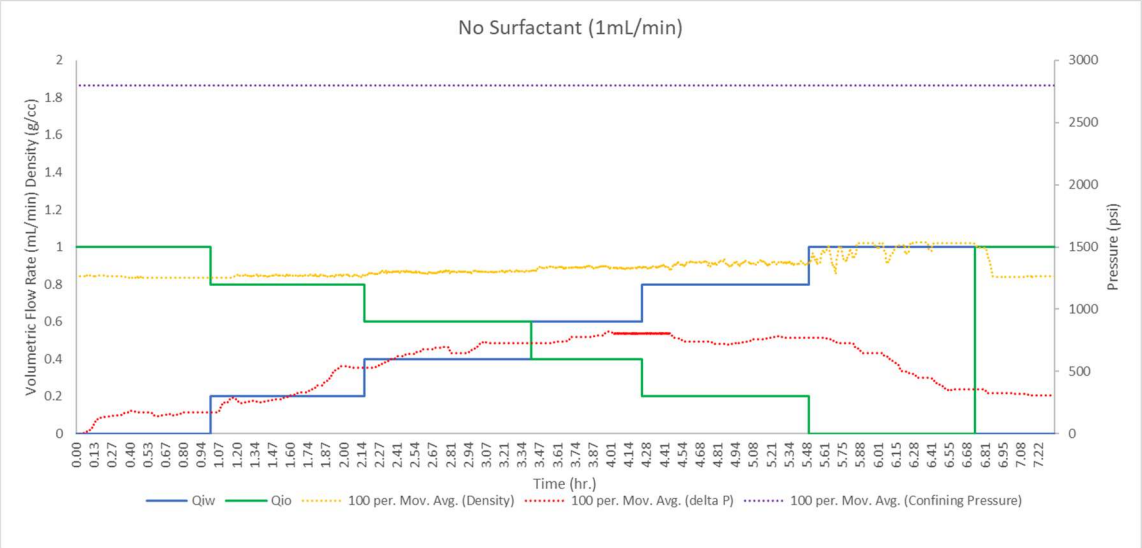

Figure 3-3 Recorded Data from Fracture Relative Permeability Test 2 for No-Surfactant

Table 3-3 Measured Fracture Relative Permeability Test 2 Data for No-Surfactant

MEASURED / READ						
$Q_{w\text{-}in}$ (mL/min)	$Q_{o\text{-}in}$ (mL/min)	P_{in} (psi)	P_{out} (psi)	ΔP (psi)	$M_{m\text{-}out}$ (g/min)	$\rho_{m\text{-}out}$ (g/mL)
0.00	1.00	186	12	174	0.8	0.80
0.20	0.80	542	12	530	0.84	0.84
0.40	0.60	741	11	730	0.88	0.88
0.60	0.40	815	10	805	0.92	0.92
0.80	0.20	778	8	770	0.96	0.96
1.00	0.00	368	7	361	1	1.00
0.00	1.00	318	11	307	0.8	0.80

Table 3-4 Calculated Fracture Relative Permeability Test 2 Data for No- Surfactant

Calculated						
Fo	Fw	Sw	Keo (md)	Kew (md)	Kro	Krw
1	0	0.00	570.04	0.00	1.00	0.00
1	0	0.11	323.09	0.00	0.57	0.00
0.8	0.2	0.34	149.72	31.19	0.26	0.05
0.6	0.4	0.43	81.52	45.29	0.14	0.08
0.4	0.6	0.54	49.29	61.61	0.09	0.11
0.2	0.8	0.61	25.76	85.87	0.05	0.15
0	1	0.82	0.00	228.96	0.00	0.40

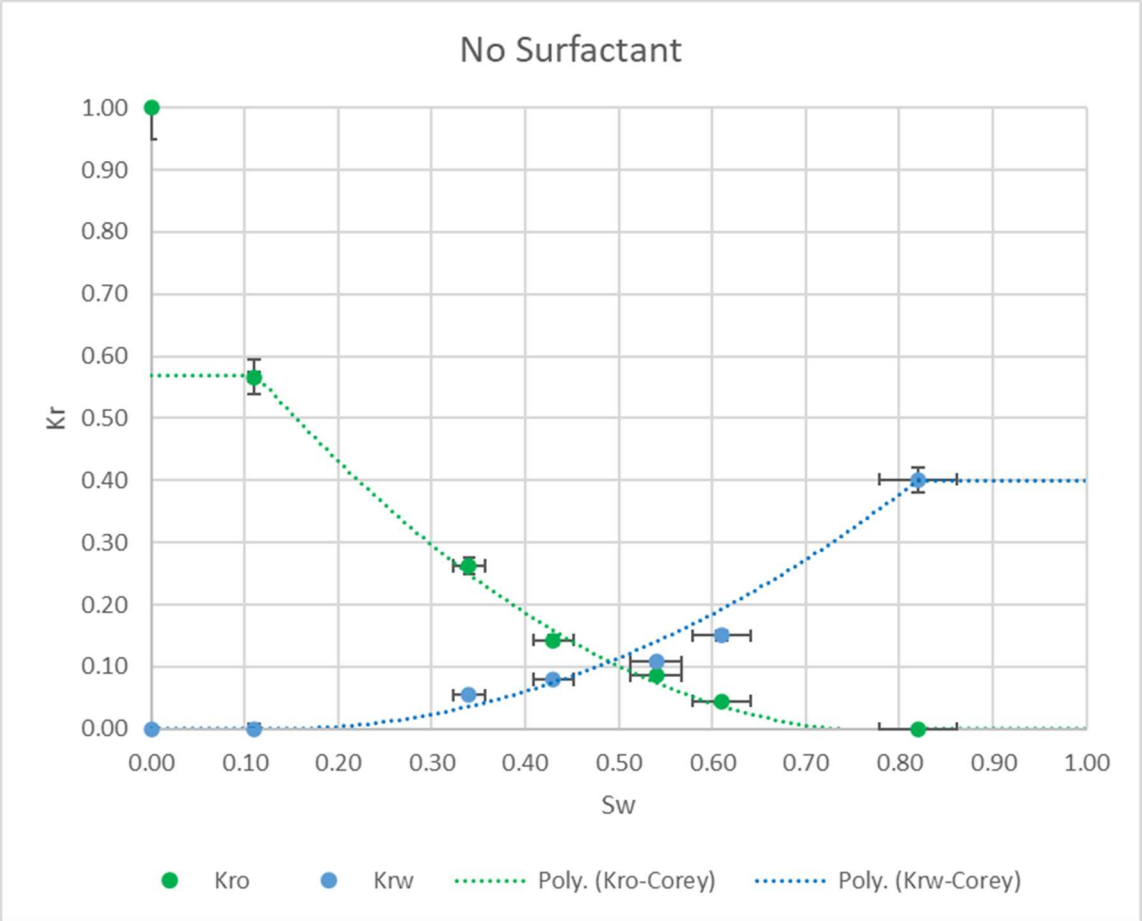

Figure 3-4 Calculated Fracture Relative Permeability Curve and Corey Fit for Test 2 No-Surfactant

Figure 3-5 presents the comparison of both tests conducted with no surfactant plotted on a fracture relative permeability curve.

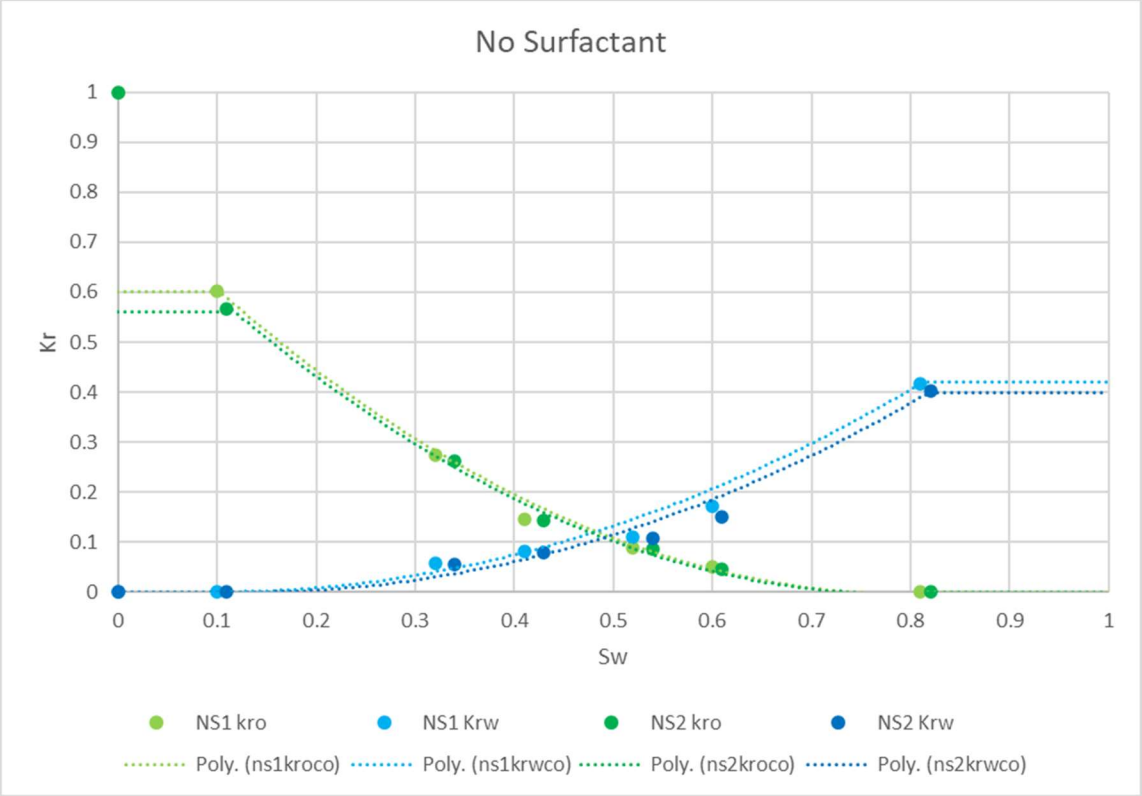

Figure 3-5 Calculated Fracture Relative Permeability Curves and Corey Fit for Comparison of No-Surfactant Test

Figure 3-6 shows the recorded data for the third test conducted with surfactant A and Table 3-5 summarizes the data measured. Table 3-6 displays a summary of the calculated relative permeabilities, and Figure 3-7 presents the relative permeability curve produced.

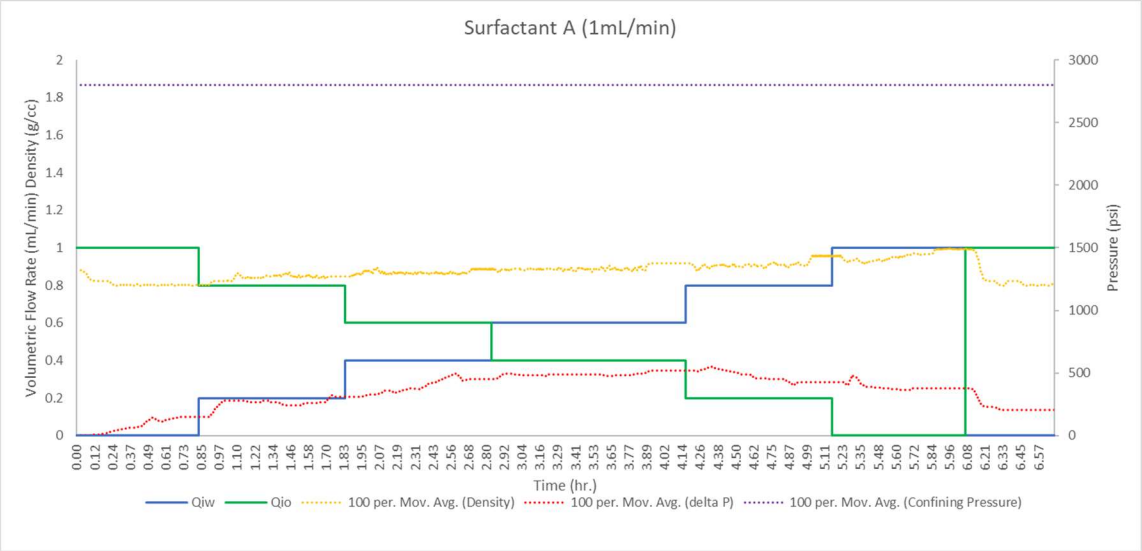

Figure 3-6 Recorded Data from Fracture Relative Permeability Test 1 for Surfactant A

Table 3-5 Measured Fracture Relative Permeability Test 1 Data for Surfactant A

MEASURED / READ						
$Q_{w\text{-}in}$ (mL/min)	$Q_{o\text{-}in}$ (mL/min)	P_{in} (psi)	P_{out} (psi)	ΔP (psi)	$M_{m\text{-}out}$ (g/min)	$\rho_{m\text{-}out}$ (g/mL)
0.00	1.00	158	10	148	0.8	0.80
0.20	0.80	321	10	311	0.84	0.84
0.40	0.60	458	9	449	0.88	0.88
0.60	0.40	526	9	517	0.92	0.92
0.80	0.20	432	8	424	0.96	0.96
1.00	0.00	385	8	377	1	1.00
0.00	1.00	215	11	204	0.8	0.80

Table 3-6 Calculated Fracture Relative Permeability Test 1 Data for Surfactant A

Calculated						
Fo	Fw	Sw	Keo (md)	Kew (md)	Kro	Krw
1	0	0.00	670.19	0.00	1.00	0.00
1	0	0.13	486.21	0.00	0.73	0.00
0.8	0.2	0.4	255.14	53.15	0.38	0.08
0.6	0.4	0.52	132.54	73.63	0.20	0.11
0.4	0.6	0.61	76.74	95.92	0.11	0.14
0.2	0.8	0.75	46.79	155.95	0.07	0.23
0	1	0.87	0.00	219.24	0.00	0.33

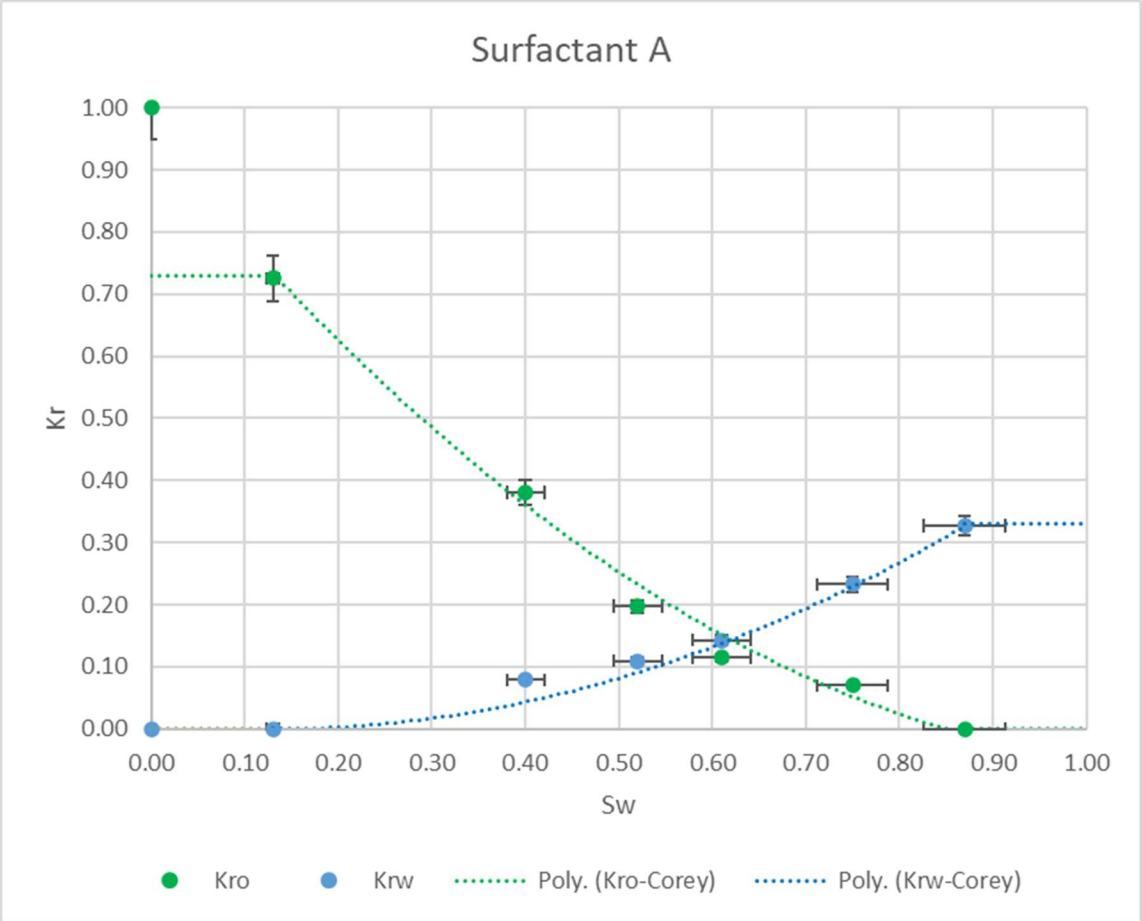

Figure 3-7 Calculated Fracture Relative Permeability Curve and Corey Fit for Test 1 Surfactant A

Figure 3-8 shows the recorded data for the fourth test conducted with surfactant A and Table 3-7 summarizes the data measured. Table 3-8 displays a summary of the calculated relative permeabilities, and Figure 3-9 presents the relative permeability curve produced.

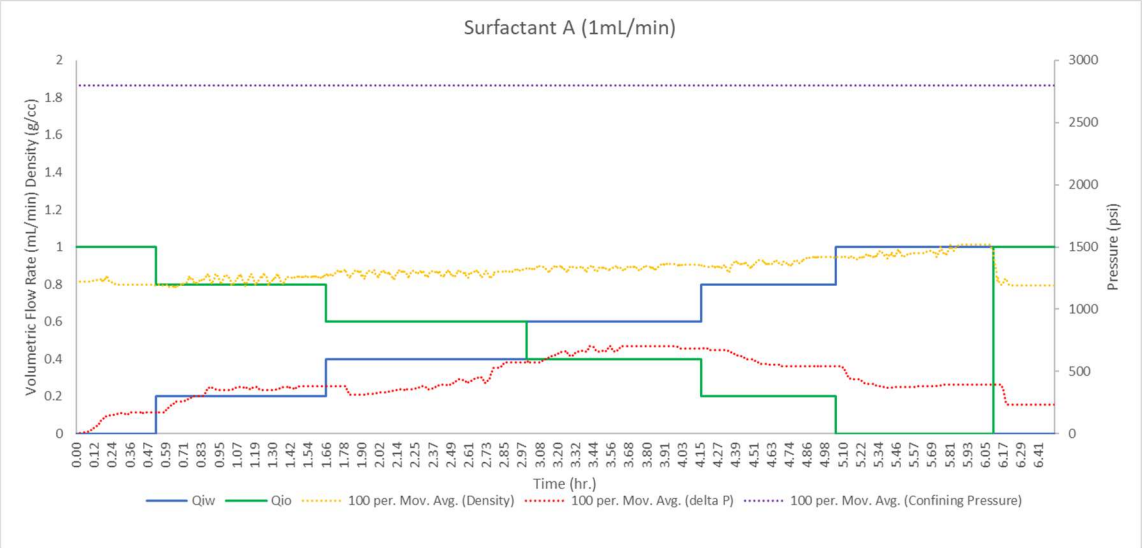

Figure 3-8 Recorded Data from Fracture Relative Permeability Test 2 for Surfactant A

Table 3-7 Measured Fracture Relative Permeability Test 2 Data for Surfactant A

MEASURED / READ						
$Q_{w\text{-}in}$ (mL/min)	$Q_{o\text{-}in}$ (mL/min)	P_{in} (psi)	P_{out} (psi)	ΔP (psi)	$M_{m\text{-}out}$ (g/min)	$\rho_{m\text{-}out}$ (g/mL)
0.00	1.00	181	10	171	0.8	0.80
0.20	0.80	389	10	379	0.84	0.84
0.40	0.60	584	9	575	0.88	0.88
0.60	0.40	695	9	686	0.92	0.92
0.80	0.20	553	8	545	0.96	0.96
1.00	0.00	398	7	391	1	1.00
0.00	1.00	244	10	234	0.8	0.80

Table 3-8 Calculated Fracture Relative Permeability Test 2 Data for Surfactant A

Calculated						
Fo	Fw	Sw	Keo (md)	Kew (md)	Kro	Krw
1	0	0.00	580.04	0.00	1.00	0.00
1	0	0.12	423.88	0.00	0.73	0.00
0.8	0.2	0.41	209.37	43.62	0.36	0.08
0.6	0.4	0.53	103.50	57.50	0.18	0.10
0.4	0.6	0.62	57.84	72.29	0.10	0.12
0.2	0.8	0.75	36.40	121.33	0.06	0.21
0	1	0.86	0.00	211.39	0.00	0.36

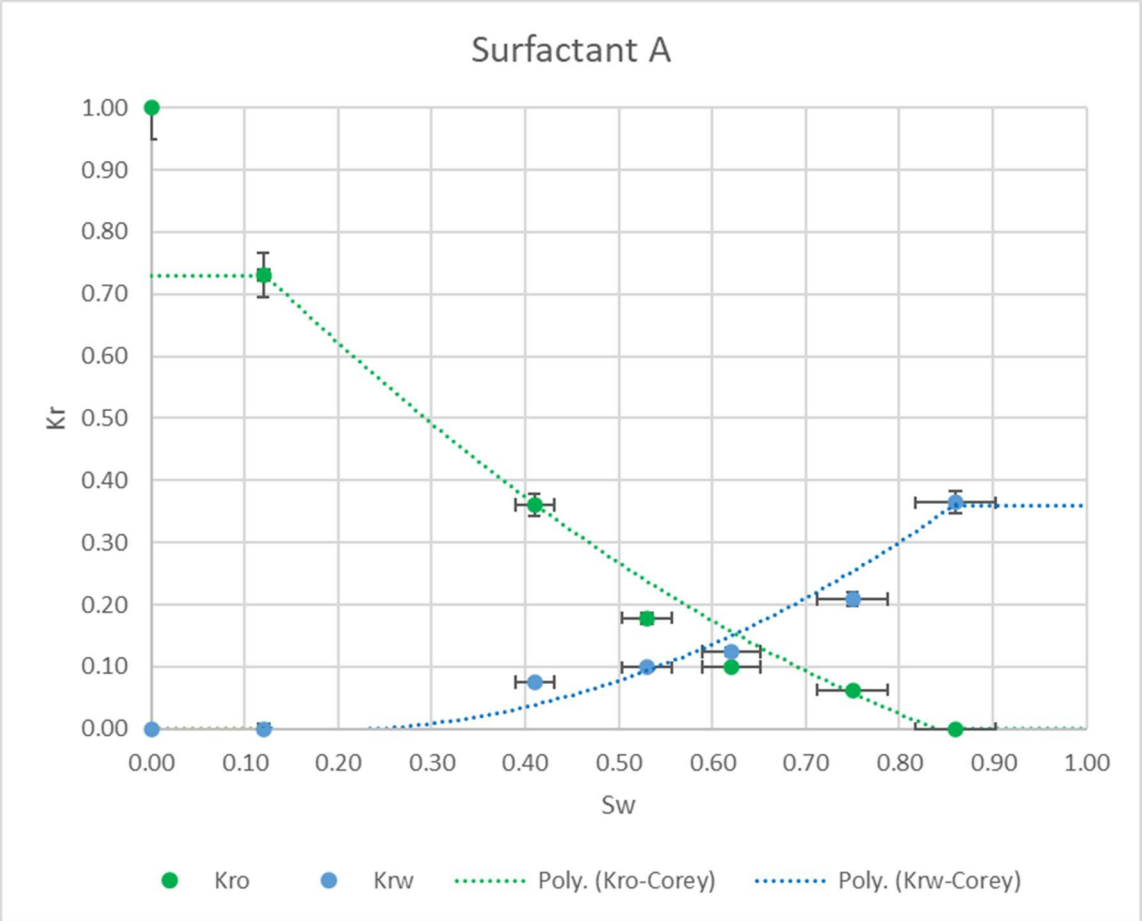

Figure 3-9 Calculated Fracture Relative Permeability Curve and Corey Fit for Test 2 Surfactant A

Figure 3-10 presents the comparison of both tests conducted with surfactant A plotted on a fracture relative permeability curve.

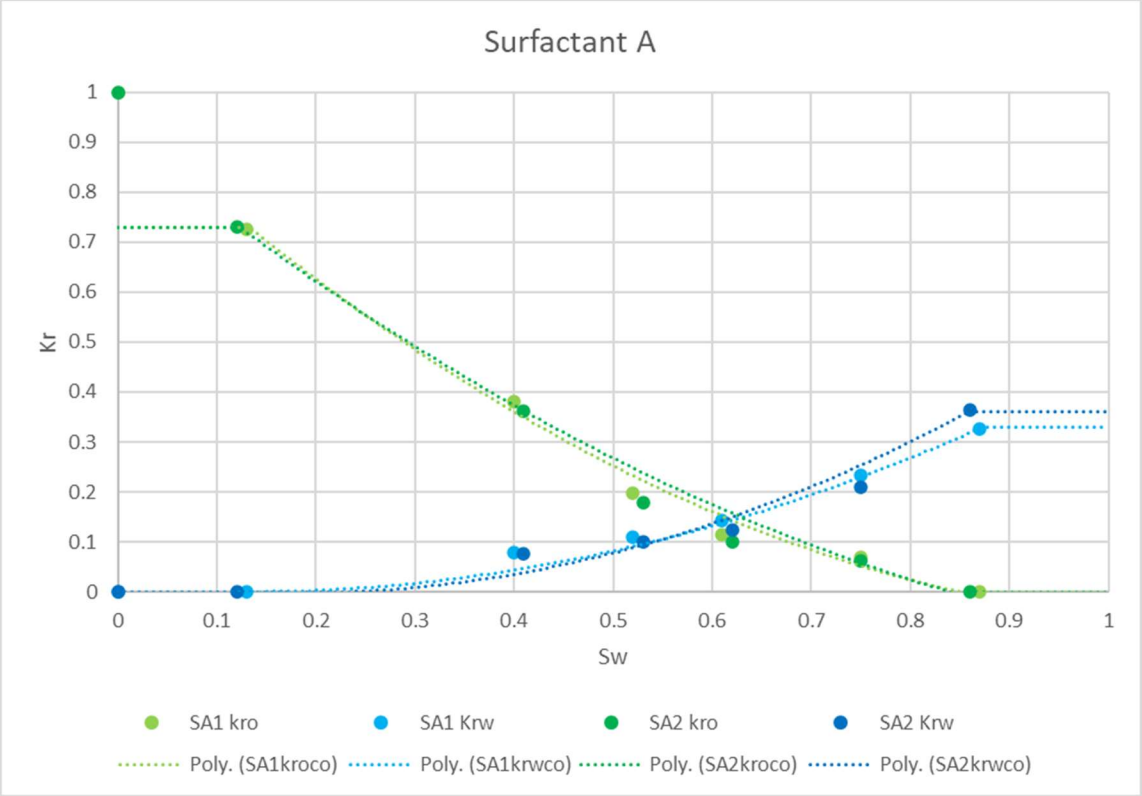

Figure 3-10 Calculated Fracture Relative Permeability Curves and Corey Fit for Comparison of Surfactant A Test

Figure 3-11 shows the recorded data for the fifth test conducted with surfactant B, and Table 3-9 summarizes the data measured. Table 3-10 displays a summary of the calculated relative permeabilities, and Figure 3-12 presents the relative permeability curve produced.

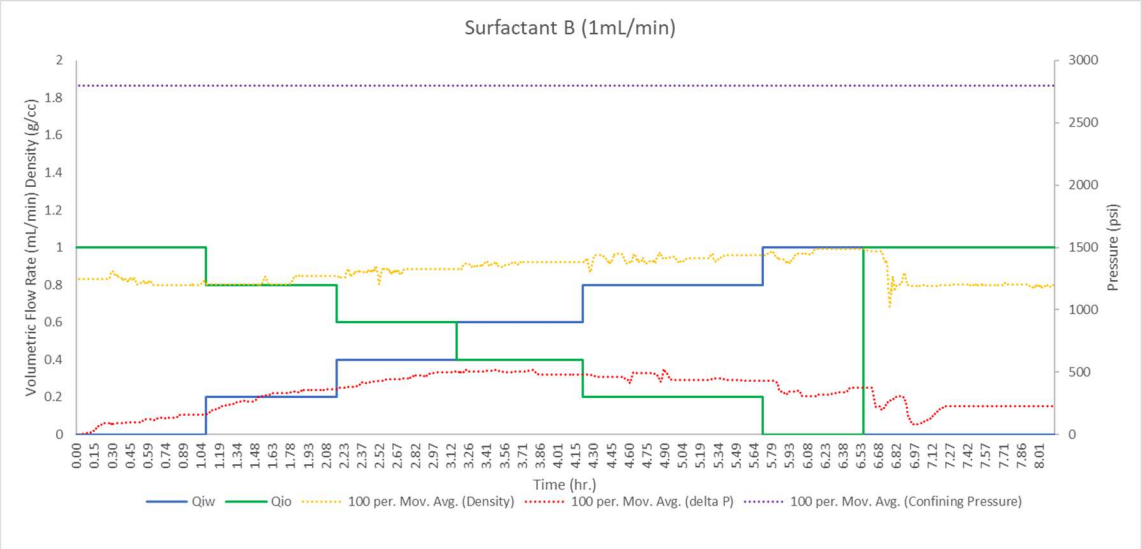

Figure 3-11 Recorded Data from Fracture Relative Permeability Test 1 for Surfactant B

Table 3-9 Measured Fracture Relative Permeability Test 1 Data for Surfactant B

MEASURED / READ						
$Q_{w\text{-}in}$ (mL/min)	$Q_{o\text{-}in}$ (mL/min)	P_{in} (psi)	P_{out} (psi)	ΔP (psi)	$M_{m\text{-}out}$ (g/min)	$\rho_{m\text{-}out}$ (g/mL)
0.00	1.00	170	7	163	0.8	0.80
0.20	0.80	363	4	359	0.84	0.84
0.40	0.60	505	4	501	0.88	0.88
0.60	0.40	485	4	481	0.92	0.92
0.80	0.20	433	2	431	0.96	0.96
1.00	0.00	380	2	378	1	1.00
0.00	1.00	229	4	225	0.8	0.80

Table 3-10 Calculated Fracture Relative Permeability Test 1 Data for Surfactant B

Calculated						
Fo	Fw	Sw	Keo (md)	Kew (md)	Kro	Krw
1	0	0.00	608.51	0.00	1.00	0.00
1	0	0.12	440.83	0.00	0.72	0.00
0.8	0.2	0.35	221.03	46.05	0.36	0.08
0.6	0.4	0.48	118.79	65.99	0.20	0.11
0.4	0.6	0.56	82.48	103.10	0.14	0.17
0.2	0.8	0.69	46.03	153.42	0.08	0.25
0	1	0.84	0.00	218.66	0.00	0.36

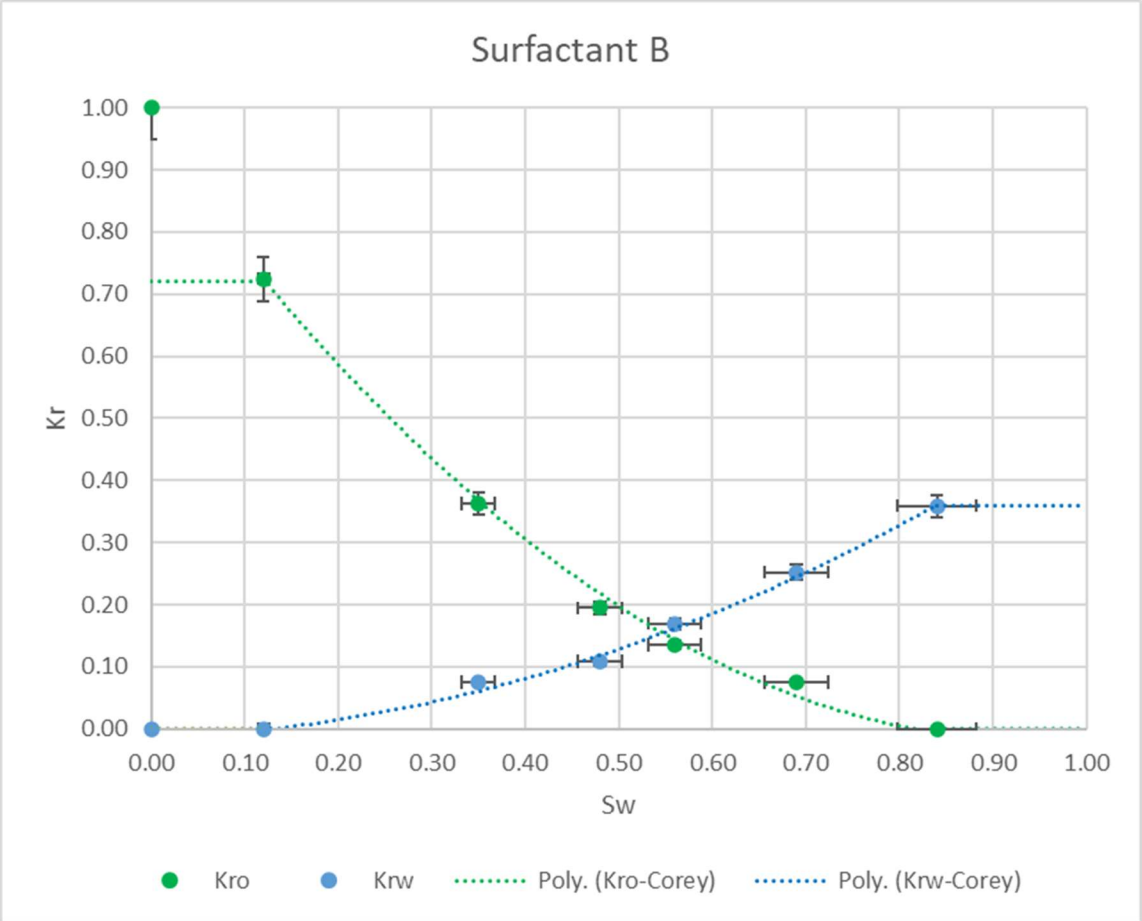

Figure 3-12 Calculated Fracture Relative Permeability Curve and Corey Fit for Test 1 Surfactant B

Figure 3-13 shows the recorded data for the sixth test conducted with surfactant B, and Table 3-11 summarizes the data measured. Table 3-12 displays a summary of the calculated relative permeabilities, and Figure 3-14 presents the relative permeability curve produced.

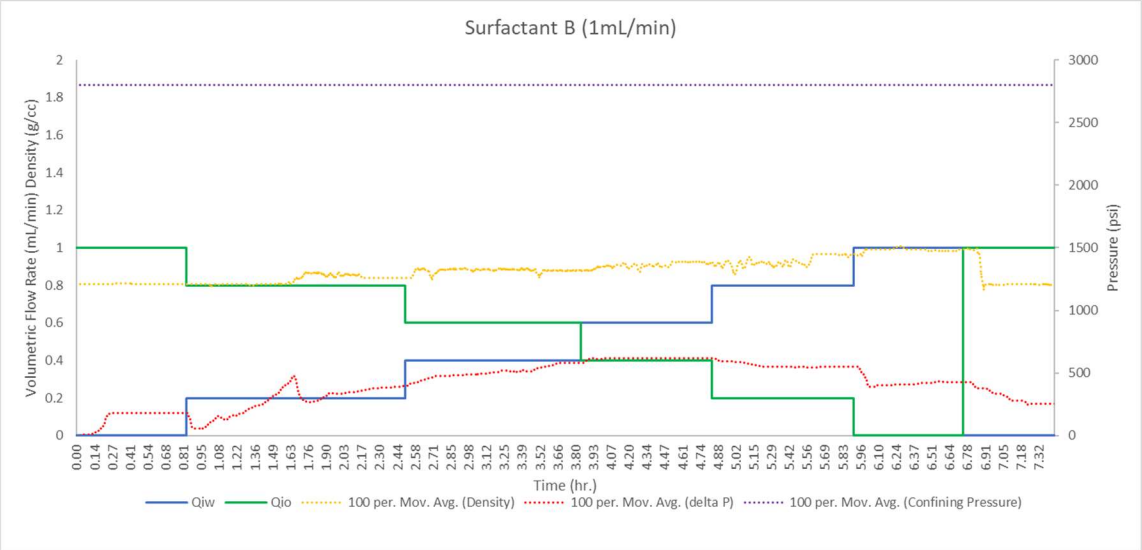

Figure 3-13 Recorded Data from Fracture Relative Permeability Test 2 for Surfactant B

Table 3-11 Measured Fracture Relative Permeability Test 2 Data for Surfactant B

MEASURED / READ						
$Q_{w\text{-}in}$ (mL/min)	$Q_{o\text{-}in}$ (mL/min)	P_{in} (psi)	P_{out} (psi)	ΔP (psi)	$M_{m\text{-}out}$ (g/min)	$\rho_{m\text{-}out}$ (g/mL)
0.00	1.00	183	5	178	0.8	0.80
0.20	0.80	400	6	394	0.84	0.84
0.40	0.60	588	6	582	0.88	0.88
0.60	0.40	622	5	617	0.92	0.92
0.80	0.20	550	4	546	0.96	0.96
1.00	0.00	426	2	424	1	1.00
0.00	1.00	256	4	252	0.8	0.80

Table 3-12 Calculated Fracture Relative Permeability Test 2 Data for Surfactant B

Calculated						
Fo	Fw	Sw	Keo (md)	Kew (md)	Kro	Krw
1	0	0.00	557.23	0.00	1.00	0.00
1	0	0.11	393.60	0.00	0.71	0.00
0.8	0.2	0.36	201.40	41.96	0.36	0.08
0.6	0.4	0.47	102.26	56.81	0.18	0.10
0.4	0.6	0.55	64.30	80.38	0.12	0.14
0.2	0.8	0.68	36.33	121.10	0.07	0.22
0	1	0.85	0.00	194.94	0.00	0.35

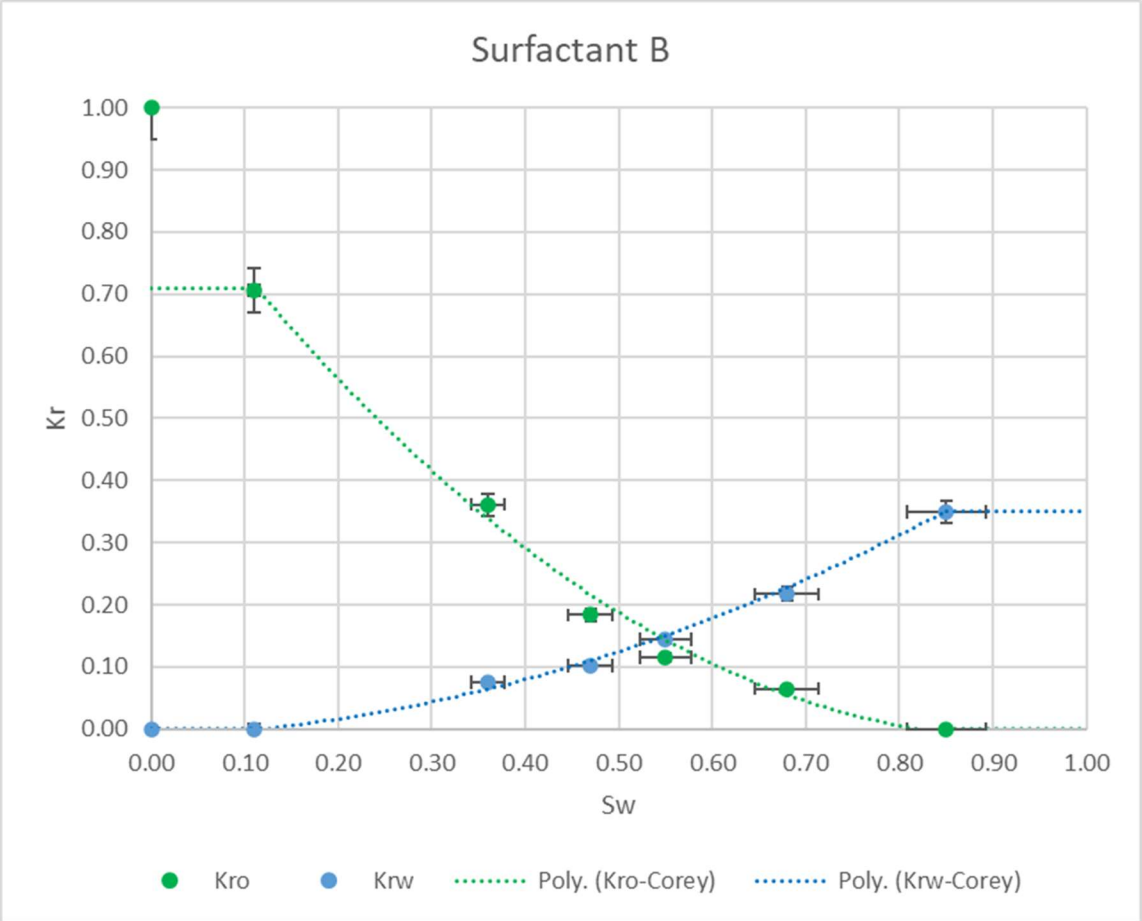

Figure 3-14 Calculated Fracture Relative Permeability Curve and Corey Fit for Test 2 Surfactant B

Figure 3-15 presents the comparison of both tests conducted with surfactant B plotted on a fracture relative permeability curve.

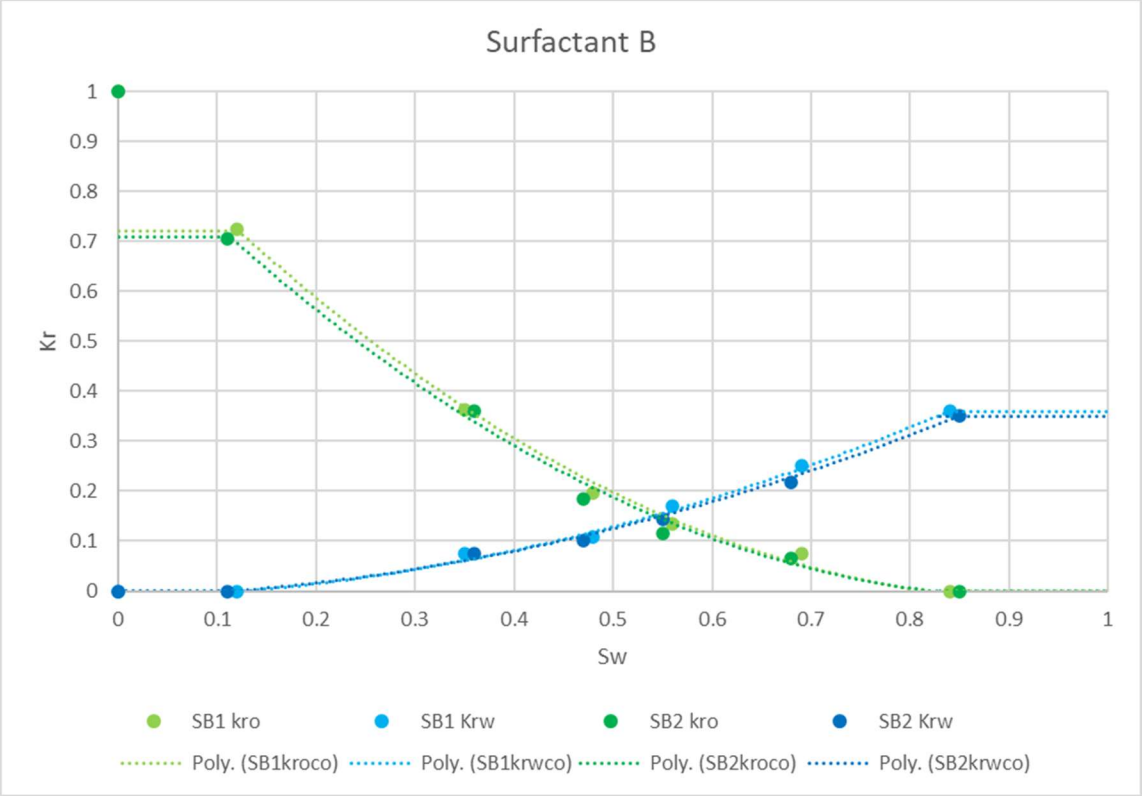

Figure 3-15 Calculated Fracture Relative Permeability Curves and Corey Fit for Comparison of Surfactant B Test

Figure 3-16 shows the recorded data for the seventh test conducted with surfactant C and Table 3-13 summarizes the data measured. Table 3-14 displays a summary of the calculated relative permeabilities, and Figure 3-17 presents the relative permeability curve produced.

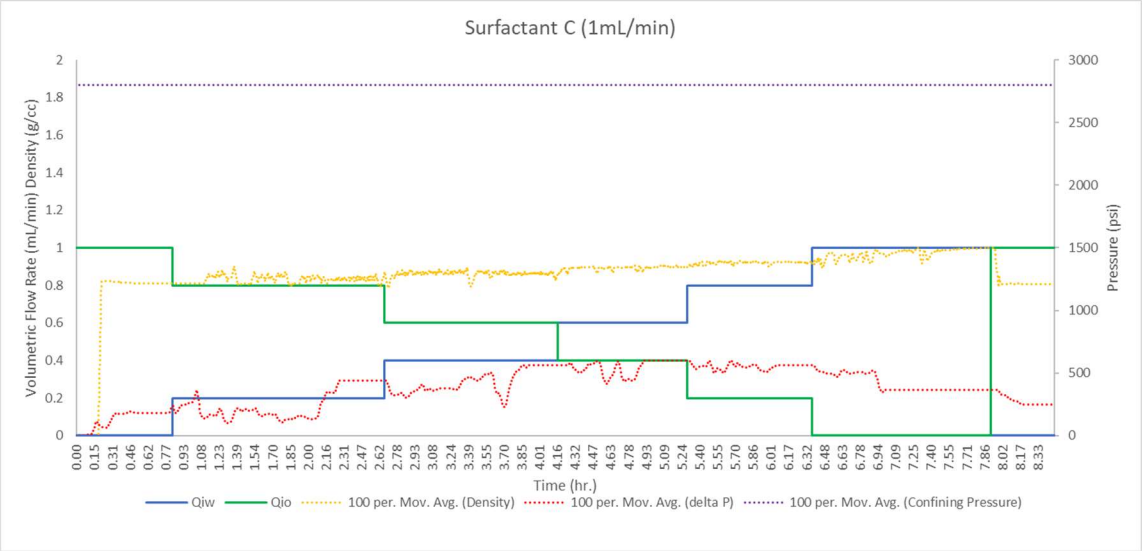

Figure 3-16 Recorded Data from Fracture Relative Permeability Test 1 for Surfactant C

Table 3-13 Measured Fracture Relative Permeability Test 1 Data for Surfactant C

MEASURED / READ						
$Q_{w\text{-}in}$ (mL/min)	$Q_{o\text{-}in}$ (mL/min)	P_{in} (psi)	P_{out} (psi)	ΔP (psi)	$M_{m\text{-}out}$ (g/min)	$\rho_{m\text{-}out}$ (g/mL)
0.00	1.00	180	10	170	0.8	0.80
0.20	0.80	450	10	440	0.84	0.84
0.40	0.60	570	10	560	0.88	0.88
0.60	0.40	608	10	598	0.92	0.92
0.80	0.20	565	7	558	0.96	0.96
1.00	0.00	372	4	368	1	1.00
0.00	1.00	258	10	248	0.8	0.80

Table 3-14 Calculated Fracture Relative Permeability Test 1 Data for Surfactant C

Calculated						
Fo	Fw	Sw	Keo (md)	Kew (md)	Kro	Krw
1	0	0.00	583.46	0.00	1.00	0.00
1	0	0.13	399.95	0.00	0.69	0.00
0.8	0.2	0.36	180.34	37.57	0.31	0.06
0.6	0.4	0.49	106.27	59.04	0.18	0.10
0.4	0.6	0.58	66.35	82.93	0.11	0.14
0.2	0.8	0.7	35.55	118.50	0.06	0.20
0	1	0.83	0.00	224.60	0.00	0.38

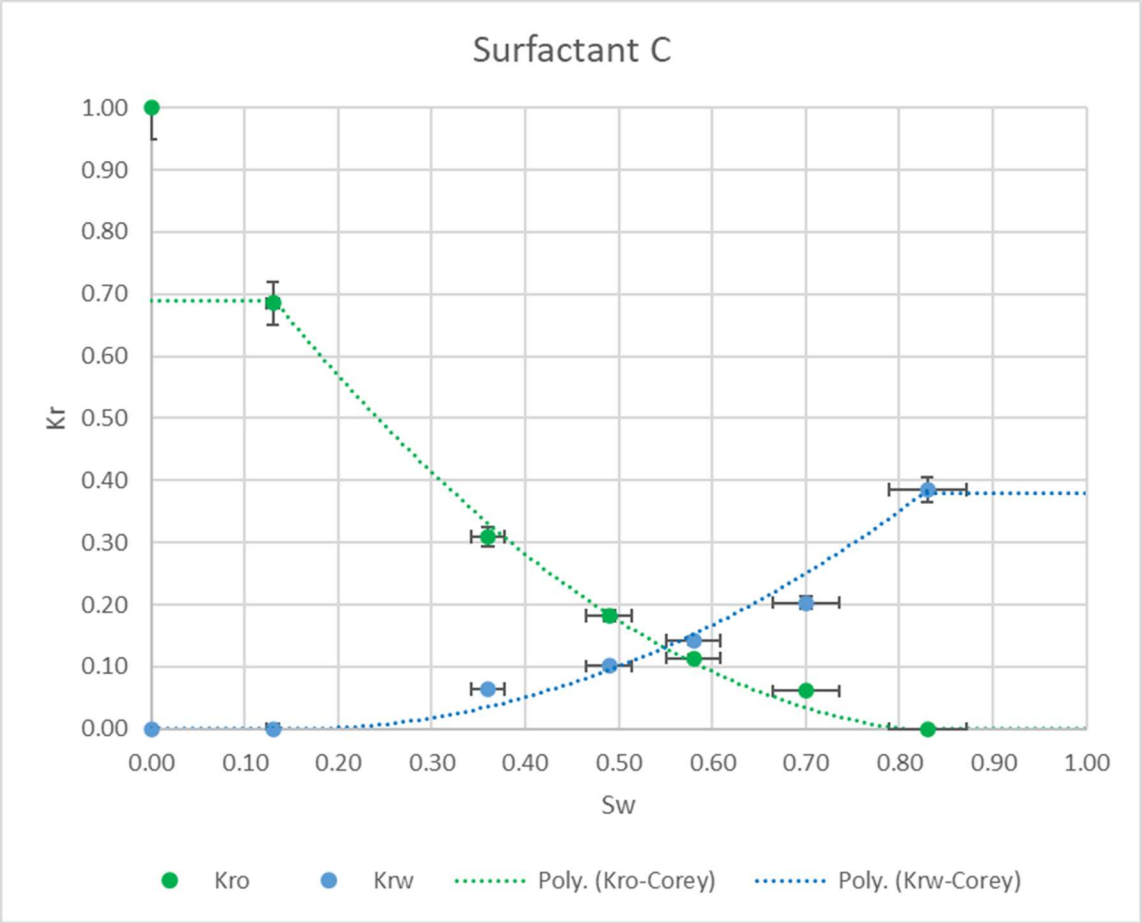

Figure 3-17 Calculated Fracture Relative Permeability Curve and Corey Fit for Test 1 Surfactant C

Figure 3-18 shows the recorded data for the eighth test conducted with surfactant C and Table 3-15 summarizes the data measured. Table 3-16 displays a summary of the calculated relative permeabilities, and Figure 3-19 presents the relative permeability curve produced.

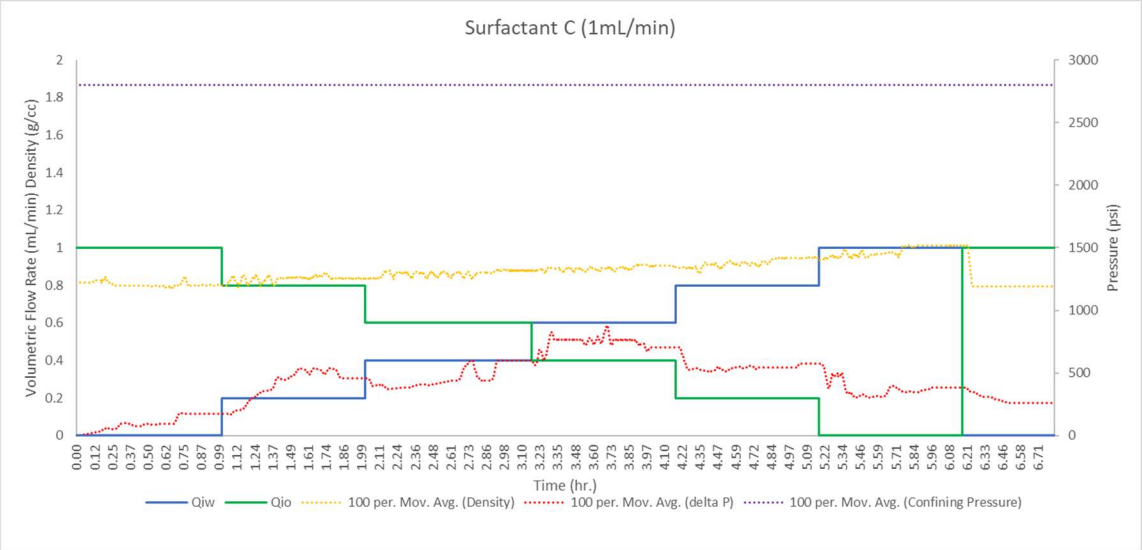

Figure 3-18 Recorded Data from Fracture Relative Permeability Test 2 for Surfactant C

Table 3-15 Measured Fracture Relative Permeability Test 2 Data for Surfactant C

MEASURED / READ						
$Q_{w\text{-}in}$ (mL/min)	$Q_{o\text{-}in}$ (mL/min)	P_{in} (psi)	P_{out} (psi)	ΔP (psi)	$M_{m\text{-}out}$ (g/min)	$\rho_{m\text{-}out}$ (g/mL)
0.00	1.00	185	10	175	0.8	0.80
0.20	0.80	468	10	458	0.84	0.84
0.40	0.60	604	10	594	0.88	0.88
0.60	0.40	712	9	703	0.92	0.92
0.80	0.20	587	8	579	0.96	0.96
1.00	0.00	388	6	382	1	1.00
0.00	1.00	271	10	261	0.8	0.80

Table 3-16 Calculated Fracture Relative Permeability Test 2 Data for Surfactant C

Calculated						
Fo	Fw	Sw	Keo (md)	Kew (md)	Kro	Krw
1	0	0.00	566.79	0.00	1.00	0.00
1	0	0.12	380.03	0.00	0.67	0.00
0.8	0.2	0.33	173.25	36.09	0.31	0.06
0.6	0.4	0.47	100.19	55.66	0.18	0.10
0.4	0.6	0.56	56.44	70.54	0.10	0.12
0.2	0.8	0.67	34.26	114.20	0.06	0.20
0	1	0.82	0.00	216.37	0.00	0.38

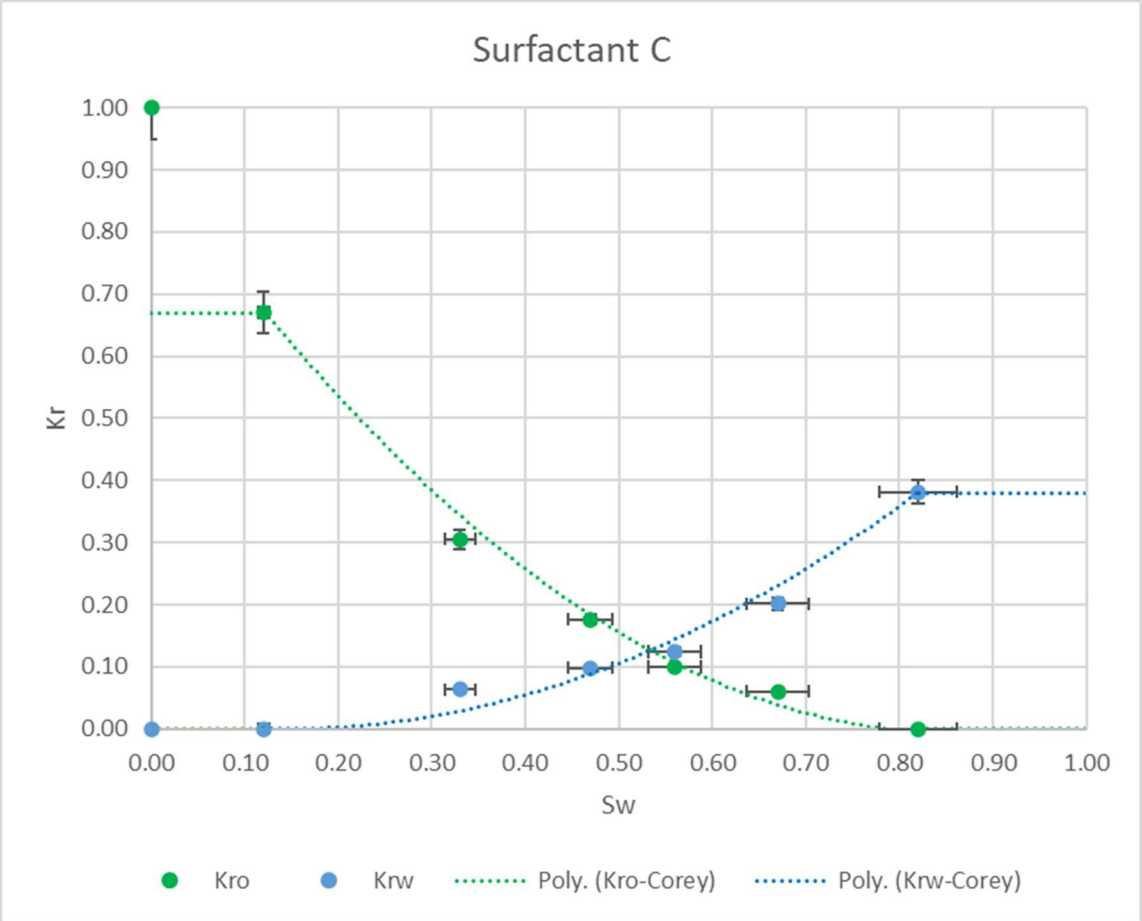

Figure 3-19 Calculated Fracture Relative Permeability Curve and Corey Fit for Test 2 Surfactant C

Figure 3-20 presents the comparison of both tests conducted with surfactant C plotted on a fracture relative permeability curve.

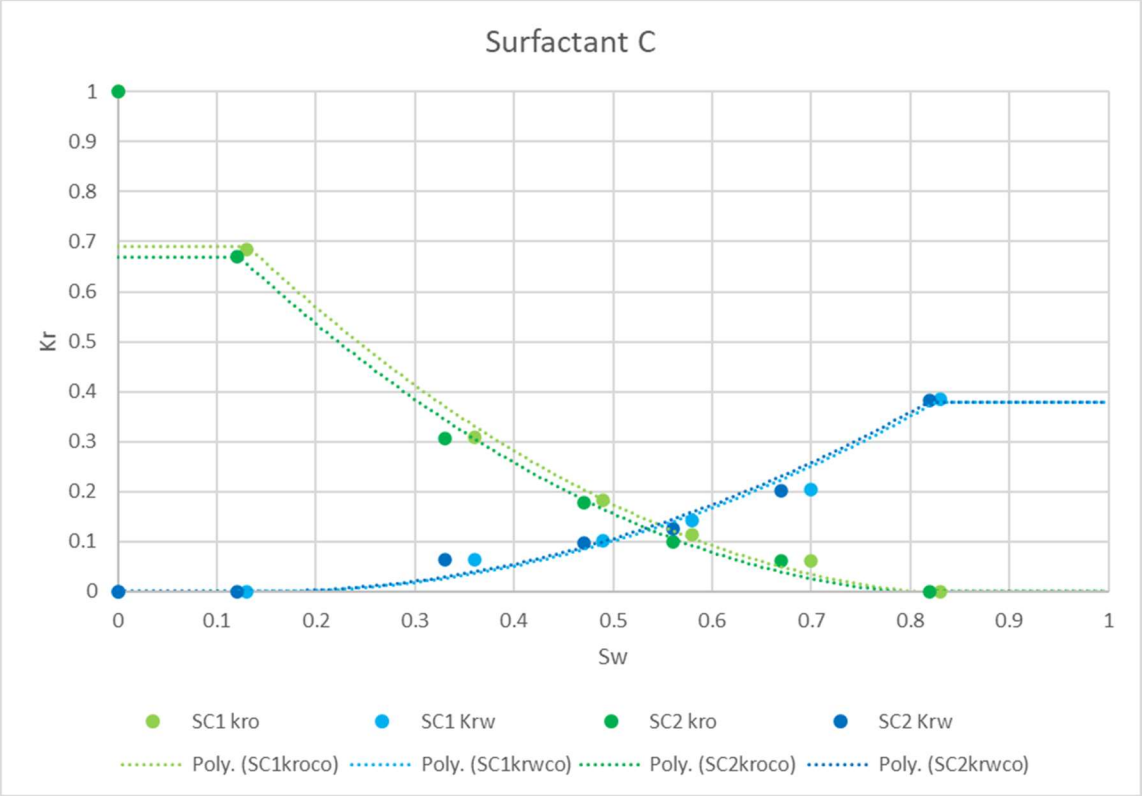

Figure 3-20 Calculated Fracture Relative Permeability Curves and Corey Fit for Comparison of Surfactant C Test

Figure 3-21 presents the average relative permeability comparison of all tests conducted with or without surfactants plotted on a fracture relative permeability curve.

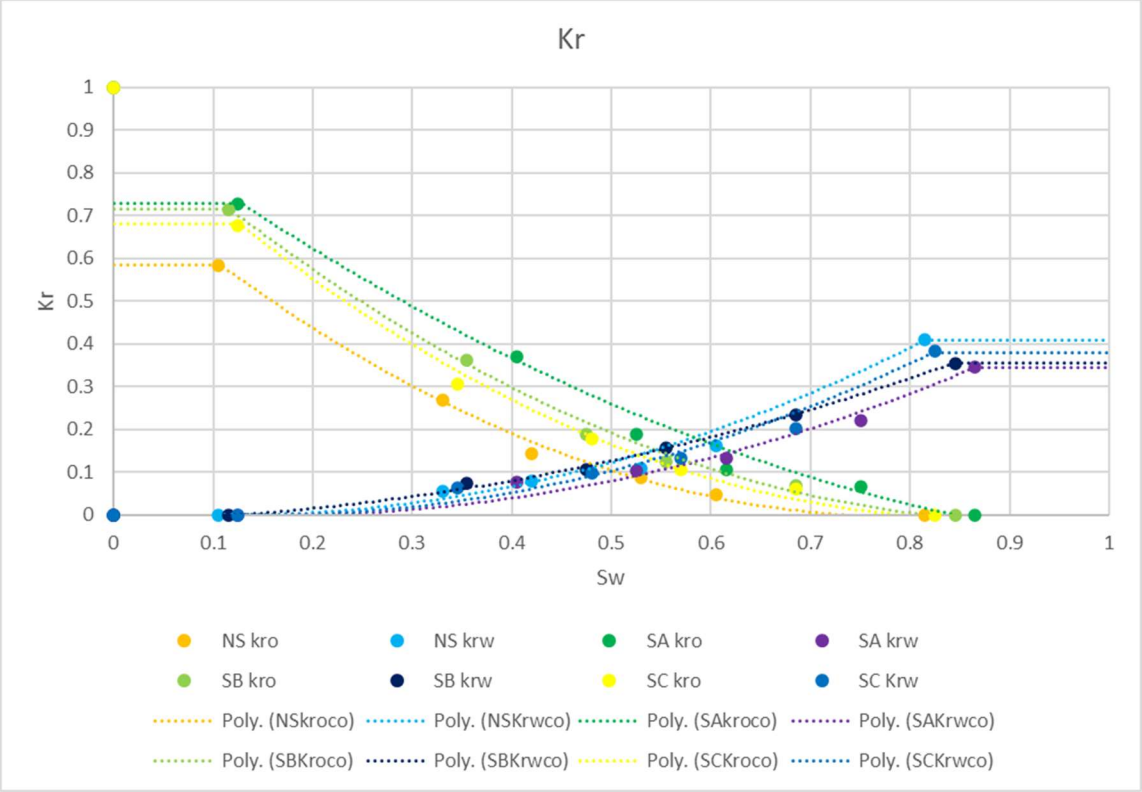

Figure 3-21 Calculated Average Fracture Relative Permeability Curves and Corey Fit for Comparison of Different Surfactants

4. CONCLUSIONS AND RECOMMENDATIONS

4.1 Conclusions

After conducting eight experiments with and without surfactants, I was able to conclude the determined relative permeability curves closely follow the generalized Brooks-Corey relationship for oil-water systems. Additionally, there was a significant difference between the oil-water only systems and the oil-water surfactant systems in the relative permeability curves. The tests with surfactants change the wettability of the fracture surface from an oil-wet to a water-wet wettability, improving oil relative permeability while decreasing water relative permeability, in a way that would be beneficial for field use. A smaller contact angle and interfacial tension improves relative permeability. Based on the findings from these experiments, this beneficial change in the oil-water relative permeability behavior in fractures has also proved that water wetting surfactants will lead to theoretical increases in initial oil production rate and cumulative oil production. Surfactant additives can significantly improve the relative permeability of oil by as much as 26%. Lastly, a high percent error in predicted oil recovery would result from the use of the straight-line relative permeability for unpropped fractures. Therefore, non-straight-line relative permeability should be used for natural unpropped fractures in future experiments and simulations.

4.2 Recommendations

My first recommendation to improve this experiment would be to run more tests with outcrop rock vs. downhole core from the Eagle Ford formation to see if results vary. Next, I recommend using fracturing fluid directly from the field to see if results vary. Then, I would recommend looking into having the cores fractured instead of being saw-cut; it would allow for a larger fracture area to be analyzed. The larger fracture area would show a more typical

mineralogy distribution as well as fracture roughness features that might have a considerable impact on the measurement of the oil-water relative permeability. Next, I recommend testing at a lower flowrate such as 0.5mL/min to combat such high pressures during the test that sometimes resulted in a longer time needed to reach steady-state. Then, I recommend replacing the current core holder with an aluminum hassler type core holder in order to be able to CT scan the test specimen during testing, as a result allowing a more accurate determination of in-situ fracture saturations. Also, the original manufacturer of the current core holder went out of business, and currently, an inlet piston is being shared because of this reason. If anything else breaks on the core holder, it will have to be replaced. Additionally, I would recommend cleaning the micromotion flowmeter after every test to prevent the clogging of lines. My final recommendation would be to find an automatic relief valve for the confining pressure.

REFERENCES

Abaci, S., Edwards, J., and Whittaker, B. 1992. Relative Permeability Measurements for Two Phase Flow in Unconsolidated Sands. *Mine Water and the Environment* 11 (2): 11-26.

Akin, S. 2001. Estimation of Fracture Relative Permeabilities from Unsteady State Corefloods. *Journal of Petroleum Science and Engineering* 30 (1): 1-14.

Brooks, R.H. and Corey, A.T. 1966. Properties of Porous Media Affecting Fluid Flow. *Journal of the Irrigation and Drainage Division* 92 (2): 61-90.

Darcy, H. 1856. Les Fontaines Publique De La Ville De Dijon. *Dalmont, Paris* 647.

Diomampo, G., Chen, C.-Y., Li, K., and Horne, R.N. 2001. Relative Permeability through Fractures. In *Proc. 27th Workshop on Geothermal Reservoir Engineering*:28-30.

Donovan, A. D., Staerker, T. S., Pramudito, A., Gardner, R., Pope, M. C., Corbett, M., Romero, A. M. 2013. A 3-D Outcrop Perspective of an Unconventional Carbonate Mudstone Reservoir. Unconventional Resources Technology Conference. doi:10.1190/urtec2013-063

Gilman, J.R. and Kazemi, H. 1983. Improvements in Simulation of Naturally Fractured Reservoirs. *Society of Petroleum Engineers Journal* 23 (04): 695-707.

Glover, P. 2010. Relative Permeability. In *Formation Evaluation Msc Course Notes*.

Guerra, D. 2017. Relative Permeability of Oil-Water Systems in Fractures. [Ph.D. Dissertation]. Texas A&M University.

Honarpour, M. and Mahmood, S. 1988. Relative-Permeability Measurements: An Overview. *Journal of Petroleum Technology* 40 (08): 963-966.

Huo, D. and Benson, S.M. 2016. Experimental Investigation of Stress-Dependency of Relative Permeability in Rock Fractures. *Transport in Porous Media*: 1-24.

Izadi, M., Shadizadeh, S.R., and Moradi, S. 2012. Experimentally Measurements of Relative Permeability in Fractured Core. *International Journal of Science & Emerging Technologies* 3 (2).

Johnson, E., Bossler, D., and Naumann, V. 1959. Calculation of Relative Permeability from Displacement Experiments. *Petroleum Transactions, AIME* 216: 370-372.

Kantzas, A., Bryan, J., & Taheri, S. 2018. Fundamentals of Fluid Flow in Porous Media - Special Core Analysis & EOR Laboratory: PERM Inc. Retrieved from https://perminc.com/resources/fundamentals-of-fluid-flow-in-porous-media/

Kasiri, N. 2011. Fracture Relative Permeability Revisited. *World Oil* 232 (10).

Mungan, N. 1972. Relative Permeability Measurements Using Reservoir Fluids. *Society of Petroleum Engineers Journal* 12 (05): 398-402.

Muskat, M., Wyckoff, R., Botset, H., and Meres, M. 1937. Flow of Gas-Liquid Mixtures through Sands. *Transactions of the AIME* 123 (01): 69-96.

Pan, X., Wong, R., and Maini, B. 1996. Steady State Two-Phase in a Smooth Parallel Fracture. In *Annual Technical Meeting*: Petroleum Society of Canada.

Pieters, D. and Graves, R. 1994. Fracture Relative Permeability: Linear or Non-Linear Function of Saturation. In *International Petroleum Conference and Exhibition of Mexico*: Society of Petroleum Engineers.

Richardson, J., Kerver, J., Hafford, J., and Osoba, J. 1952. Laboratory Determination of Relative Permeability. *Journal of Petroleum Technology* 4 (08): 187-196.

Romm, E. 1966. Flow Characteristics of Fractured Rocks. *Nedra, Moscow* 283.

Sakurai, K., Watanabe, N., Ishibashi, T., Tsuchiya, N., Ohsaki, Y., Tamagawa, T., and Yagi, M. 2013. Oil-Water Relative Permeability Curves for Fractures in Granite and Limestone at Different Intrinsic Permeabilities. In *19th Formation Evaluation Symposium of Japan*: Society of Petrophysicists and Well-Log Analysts. 115

Speyer, N., Li, K., and Horne, R. 2007. Experimental Measurement of Two-Phase Relative Permeability in Vertical Fractures. Paper presented at the Thirty-Second Workshop on Geothermal Reservoir Engineering Stanford University, Stanford, California, January 22-24, 2007. DOI: SGP-TR-183.

Tsang, Y. 1989. On Two-Phase Relative Permeability and Capillary Pressure of Rough-Walled Rock Fractures. *Lawrence Berkeley National Laboratory*.

Welge, H.J. 1952. A Simplified Method for Computing Oil Recovery by Gas or Water Drive. DOI: 10.2118/124-G

APPENDIX

Table A-1 Summary of Generalized Brooks-Corey correlation Endpoint and Corey Exponent Values for Oil-Water Relative Permeability Curves in Fractures

	Corey Model Summary for All Tests							
	Test 1				Test 2			
No Surfactant	Kro		Krw		Kro		Krw	
	Kro-swmin	1.00	Krw-sor	0.42	Kro-swmin	1.00	Krw-sor	0.40
	Sw max	1.00	Sw max	1.00	Sw max	1.00	Sw max	1.00
	Sor	0.19	Sor	0.19	Sor	0.18	Sor	0.18
	Swi	0.00	Swirr	0.10	Swi	0.00	Swirr	0.11
	Co	2.40	Cw	2.00	Co	2.50	Cw	2.10
Surfactant A	Kro		Krw		Kro		Krw	
	Kro-swmin	1.00	Krw-sor	0.33	Kro-swmin	1.00	Krw-sor	0.36
	Sw max	1.00	Sw max	1.00	Sw max	1.00	Sw max	1.00
	Sor	0.13	Sor	0.13	Sor	0.14	Sor	0.14
	Swi	0.00	Swirr	0.13	Swi	0.00	Swirr	0.12
	Co	1.60	Cw	2.00	Co	1.50	Cw	2.30
Surfactant B	Kro		Krw		Kro		Krw	
	Kro-swmin	1.00	Krw-sor	0.36	Kro-swmin	1.00	Krw-sor	0.35
	Sw max	1.00	Sw max	1.00	Sw max	1.00	Sw max	1.00
	Sor	0.16	Sor	0.16	Sor	0.15	Sor	0.15
	Swi	0.00	Swirr	0.12	Swi	0.00	Swirr	0.11
	Co	1.80	Cw	1.60	Co	1.90	Cw	1.60
Surfactant C	Kro		Krw		Kro		Krw	
	Kro-swmin	1.00	Krw-sor	0.38	Kro-swmin	1.00	Krw-sor	0.38
	Sw max	1.00	Sw max	1.00	Sw max	1.00	Sw max	1.00
	Sor	0.17	Sor	0.17	Sor	0.18	Sor	0.18
	Swi	0.00	Swirr	0.13	Swi	0.00	Swirr	0.12
	Co	1.90	Cw	2.10	Co	2.00	Cw	2.10